Title

The multi-scale damage evolution of nano-modified concrete under the cold region tunnel environment based on micromechanical model

Permalink

https://escholarship.org/uc/item/5rt430c7

Authors

Xia, Wei
Li, Wei-kang
Rao, Jia-rui
et al.

Publication Date

2025

DOI

10.1016/j.compstruct.2024.118612

Composite Structures 351 (2025) 118612

Contents lists available at ScienceDirect

Composite Structures

journal homepage: www.elsevier.com/locate/compstruct

The multi-scale damage evolution of nano-modified concrete under the cold region tunnel environment based on micromechanical model

Wei Xia [a], Wei-kang Li [a], Jia-rui Rao [a], Zong-quan Jiang [b], Jiann-wen Woody Ju [d], Sheng-ai Cui [a,c,*]

[a] *School of Civil Engineering, Southwest Jiaotong University, Chengdu 610031, China*
[b] *China Power Construction Railway Investment Group Co, LTD, Beijing 100070, China*
[c] *Sichuan Transportation Civil Engineering, Material Engineering, Technology Research Center, Chengdu 610031, China*
[d] *Department of Civil & Environmental Engineering, University of California, Los Angeles, CA 90095-1593, USA*

ARTICLE INFO

Keywords
Nano-modification
In-situ CT
Digital volume correlation
Micromechanical analysis
Generalized self-consistent model

ABSTRACT

In cold region tunnel construction environments, concrete performance often deteriorates due to consistently low temperatures. Nanomaterials, as efficient admixtures, can significantly improve the pore structure of concrete. Given the significant impact of pore structure characteristics on concrete performance in cold regions, this study investigates the effects of nanomaterial modification on concrete using a micromechanical model. In-situ CT tests on nano-modified concrete provided digital volume images of the pore structure. The region-growing algorithm (RGA) and digital volume correlation (DVC) method were used to reveal pore structure evolution. The microscopic damage during the phase transition of pore water was analyzed based on the pre-melting dynamic theory and the micromechanical model. The fatigue damage mechanism and generalized self-consistent model were employed to study the macroscopic performance. The results indicate that while nanomaterials do not significantly inhibit the formation of small pores/defects in concrete, they can effectively prevent the interconnection between pores. This suppression leads to fewer larger pores forming. However, the thinner matrix concrete around these large pores results in more severe damage.

1. Introduction

Concrete located in high plateaus and cold regions often face harsh climatic conditions, posing significant challenges to the stability and safety of tunnel structures [1]. Concrete lining in tunnels in cold regions undergoes damage and deterioration due to the cold weather condition, leading to a series of problems such as cracking and spalling of tunnel linings, subsequently causing instability in supporting structures [2]. The cold weather conditions at seepage tunnel portal in cold regions pose even greater challenges. Concrete at tunnel portal is directly subjected to external environmental conditions, enduring extremely low temperatures and significant temperature variation [3]. In cold seasons, the freezing depth of many tunnels starts from the lining surface and reaches over 1 m. Undoubtedly, the lowest temperature of the shotcrete layer for initial tunnel support will be below 0 °C. Due to the seasonal variation of groundwater in the stratum, shotcrete, being a porous material, often contains water [4]. In this situation, the shotcrete with water content is influenced by the freezing temperature, causing internal pore water to freeze and generate significant frost forces on pore walls. These forces far exceed the tensile strength of concrete and are the intrinsic driving force behind concrete damage.

Extensive research has been conducted on the mechanisms of damage and failure during the freeze process of concrete. However, there is still not a complete understanding of the freezing damage mechanism and its influencing factors. Building upon an understanding of the freeze damage process and mechanisms in rocks, Waldre et al. [5] developed a model for crack propagation in frozen rocks based on fracture mechanics and the second frost expansion theory. Hori et al. [6], on the other hand, assumed that the deterioration of rocks due to freeze is a result of pore cracking caused by the freezing and migration of water. Taber [7] pointed out the formation of ice lenses at the ice front, obtaining water from capillary streaks beneath the ice front. Everett [8] further developed the thermodynamic theory behind ice segregation in soil research. The liquid layer is maintained by van der Waals forces with forces on the

---

* Corresponding author at: School of Civil Engineering, Southwest Jiaotong University, Chengdu 610031, China.
E-mail addresses: xiawei_2020@163.com (W. Xia), 17337881238@163.com (W.-k. Li), 18706873114@163.com (Z.-q. Jiang), juj@ucla.edu (J.-w.W. Ju), shengai_cui@163.com (S.-a. Cui).

https://doi.org/10.1016/j.compstruct.2024.118612
Received 24 April 2024; Received in revised form 23 July 2024; Accepted 23 September 2024

order of tens of megapascals between its crystals and the pore wall [9]. As a result, water can flow towards the crystals, ensuring the possibility of growth. To prevent crystals from growing larger than the pores, the pore wall must match the pressure transmitted through the liquid layer. These are commonly referred to as crystallization pressures [10]. Presently, it is accepted that crystallization pressure is responsible for the majority of stresses in the material's pores [11]. The resistance to freeze in materials is primarily determined by three key factors: material properties, moisture conditions, and thermal conditions. Among these, properties such as pore structure characteristics and elastic modulus directly dictate the concrete's resistance to freezing [12].

Nanomaterials, as effective additives for concrete modification, have gained extensively attention due to their surface effects and size effects [13,14]. Currently, nano-oxides such as nano-SiO_2 and nano-TiO_2 have gradually become a major focus in concrete research. Nano particles can serve as nucleating agents for C-S-H gel, promoting the growth of C-S-H gel chains and reducing the capillary porosity in cement paste [15,16]. Specifically, nano-silica (NS), owing to its pozzolanic reactivity [17], is extensively employed as an excellent cement admixture [18,19], facilitating the hydration process [20] and enhancing the composite mesoporous structure [21]. Nano-titania (NT), due to its good chemical stability, and high photocatalytic activity, can interact with oxygen and water in cement, thereby increasing nucleation rates, elongating the average chain length of C-S-H gel, and reducing the aspect ratio of AFt [22–25]. The application of nanomaterials in cold region tunnel holds significant and promising prospects. The introduction of nanoparticles results in a denser microstructure for the cement paste and significantly improves the pore structure of concrete [26]. Xia et al. [27] conducted a study on nanomodification of shotcrete in winter construction environments, revealing that nanomaterials can significantly enhance early-stage performance. The utilization of nanomaterials for the modification of concrete in cold region tunnel engineering proves to be a viable approach for improving performance under cold weather environment. Although the addition of nanomaterials can significantly enhance the strength and other properties of concrete, there are several drawbacks to their application in concrete[28–30]. The high surface energy of nanomaterials can lead to agglomeration, which not only prevents them from functioning effectively but also becomes initiation points for internal cracks in the concrete. In other words, the addition of nanomaterials reduces the workability of the concrete, and the dispersion of nanoparticles inevitably increases the water demand. To prevent a high water-cement ratio from reducing the strength of the concrete, water-reducing agents and other additives must be used, which can alter the performance of the concrete. Additionally, while nanomaterials can fill the micro-voids in concrete, increasing its density, this overly dense structure may not be suitable for certain applications, such as insulation systems or high-temperature, high-pressure environments. In these cases, the high thermal conductivity of the dense concrete hinders effective insulation, and the overly dense structure reduces its impact resistance. Finally, the high cost and unstable mass production of nanomaterials limit their application in concrete.

However, the impact of nanomaterial modification on the pore structure of concrete and its influence on freezing damage resistance remain unclear. This lack in the mechanism investigation significantly limits the application of nanomaterials for modification in cold region tunnel concrete. Therefore, the in-situ CT test of nano-modified concrete under the cold region tunnel environment was conducted to reveal pore structure evolution in this study. The influence of nanomaterials on the pore size distribution, pore interval distribution, and elastic modulus of concrete was explored. Based on the Layered Represented Area Element (RAE) model, concrete was considered as a composition of pores and a concrete encapsulation layer at the microscopic level. The changes in pore structure resulting from the freezing process of pore water in the RAE model were investigated by the per-melting dynamics theory. Simultaneously, the fatigue damage model is employed to investigate the deterioration process of the concrete encapsulation layer. The macroscopic concrete performance degradation was investigated based on the generalized self-consistent model. Finally, based on the micromechanical damage model, the study further discusses the effects of these pore structure parameters on the performance of nano-modified concrete under the cold region tunnel environment.

2. Materials and nano-modified concrete mix proportion

To investigate the effects of nano-materials on concrete under the cold region tunnel environment, two types of nano-materials, i.e., nano-silica (NS) and nano-titan (NT) were employed in this study. Based on our previous study, the optimum doses of nano-silica and nano-titian were determined as 2 % [27] and 1 % by binder mass, respectively. The SEM images of nano-silica (featuring a size of 20 ~ 50 nm) and nano-titian (featuring a size of 20 ± 5 nm) were rendered in Fig. 1.

The Ordinary Portland Cement (P.O 42.5) was adopted as binder of concrete. Machine-made sand and crushed stone were employed as fine aggregate and coarse aggregate, respectively. The mix proportions for all groups are provided in Table 1.

Three 100 × 100 × 400 mm prismatic specimens and one 40 × 40 × 80 mm specimen for each group were prepared for macroscopic performance testing and in-situ CT testing, respectively. After molding, the specimens were cured in a simulated cold region environment for 28 days before testing. At 0 days, 25 days, and 100 days of service in the simulated cold region environment, the mass and resonant frequency of the prismatic specimens were measured, and in-situ CT scanning (featuring the precision of 55.6 μm) was performed on the 40 × 40 × 80 mm specimen.

3. The simulation of cold region tunnel environment

In cold region tunnel construction environments, the performance of concrete within the tunnel is highly susceptible to the influence of extreme weather [31]. Therefore, to ensure the strength development of concrete, it is typically necessary to implement insulation measures for the concrete inside the tunnel under construction, ensuring that the temperature for concrete construction and curing is not lower than 5 °C [32]. Common insulation measures inside tunnels are shown in Fig. 2.

This method involves suspending a thermal insulation shed at the portal of the tunnel and adopting temporary stove every 50 m to maintain the temperature for concrete curing, thereby ensuring construction quality. Once the construction of the tunnel lining system is completed, the insulation measures will be removed. At this point, the concrete, especially at the tunnel portal, will be directly exposed to the cold region environment. The service environment for the concrete at this stage becomes more severe and destructive. The environmental parameters for concrete service design located in the cold region [33] are shown in Fig. 3.

Based on the survey research, the environmental conditions with the lowest temperature of −20 °C and the highest temperature of 3 °C were selected as the destructive environment for concrete at the tunnel portal. Therefore, in this study, the curing temperature of concrete specimens is set to a constant 5 °C. After curing the concrete specimens at 5 °C for 28 days, they are transferred to a freeze–thaw cycle environment with the highest daily temperature set at 3 °C and the lowest at −20 °C for durability testing.

4. The *meso*-performance deterioration process of concrete under the cold region tunnel environment

As concrete continues to be used in the cold region tunnel environment, research is conducted on the deterioration of its macroscopic performance by measuring the mass and resonant frequency of concrete specimens at different service times. The loss rates of mass and resonant frequencies for each condition are determined from representative values of three specimens, as illustrated in Fig. 4.

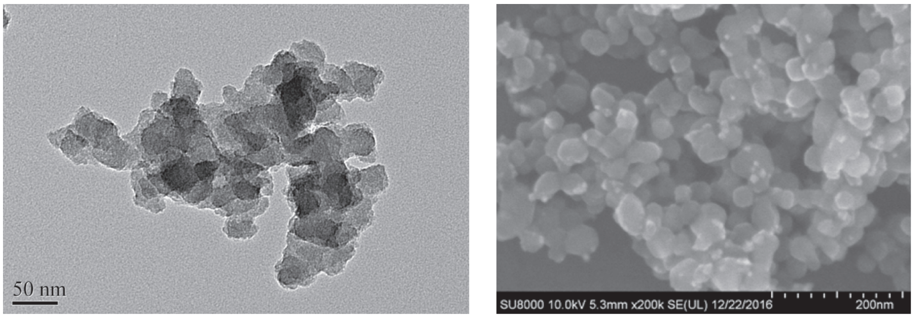

(a) SEM image of nano-silica

(b) SEM image of nano-titian

Fig. 1. The SEM images of nano-materials.

Table 1
Mix proportions of concrete. (unit: kg/m^3).

MIX. ID	Binder	Machine-made sand	Crushed stone	Water	Accelerator
CC	400(OPC)	867	769	201	21
NT	396(OPC) + 4(NT)	867	769	201	21
NS	392(OPC) + 8(NS)	867	769	201	21

As shown in the Fig. 4, the mass and resonant frequency loss rates of concrete specimens increase gradually with the service time in the cold region environment. The control concrete (CC) group exhibits significantly higher mass and resonant frequency loss rates than the nano-modified concrete. According to the GB/T 50,082 standard [34], concrete is considered to have failed when the mass loss rate reaches 5 %. Therefore, by fitting the mass loss curves in the Fig. 4, the failure ages of all groups can be predicted, as shown in the Table 2.

From the Table 2, it is evident that the CC group has the shortest lifespan in the cold region environment, while the concrete lifespan is significantly improved by using nano-modified. The in-situ CT scans on concrete specimens for each group at 0, 25, and 100 days in the cold region tunnel environment were conducted. After three-dimensional reconstruction, the precision of the digital volume image for each group was determined as 55.6 μm. In order to determine the development of each pore within the concrete under the cold region tunnel environment, it was necessary to label and extract the pores in the digital volume images obtained by applying an image segmentation method. Therefore, the global threshold segmentation method based on a fixed threshold was not suitable in this case [35]. Instead, an automatic seed point selection region-growing algorithm (RGA) to label and extract all the pores in the concrete, obtaining the voxel coordinates at the boundaries of all pores, was employed. This allowed to track the changes in the pore structure within the concrete under the cold region tunnel environment.

4.1. Image segregation process of concrete 3D digital volume based on the region growing algorithm (RGA)

The region growing algorithm is a commonly employed approach, especially when no prior knowledge can be utilized, and it can achieve optimal performance for segmenting complex images. The basic idea of the RGA used in this study is to segment pixel points in a three-dimensional grayscale image into pore labels and solid labels, starting from a single pixel point (seed point) in the three-dimensional grayscale matrix and iteratively expanding similar pixel points, merging them together [36]. It gradually grows the region by merging adjacent voxels

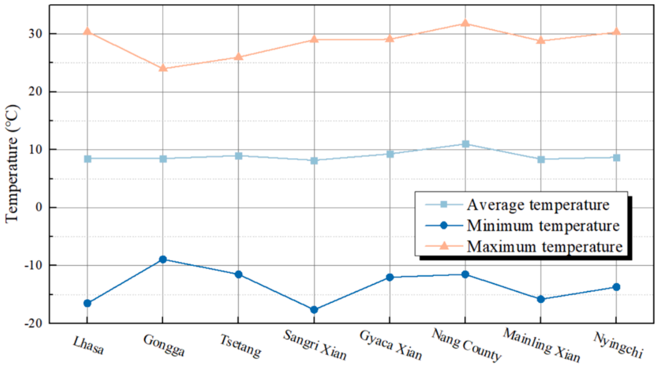

Fig. 3. Environmental parameter of major cites along the Sichuan-Tibet Railway.

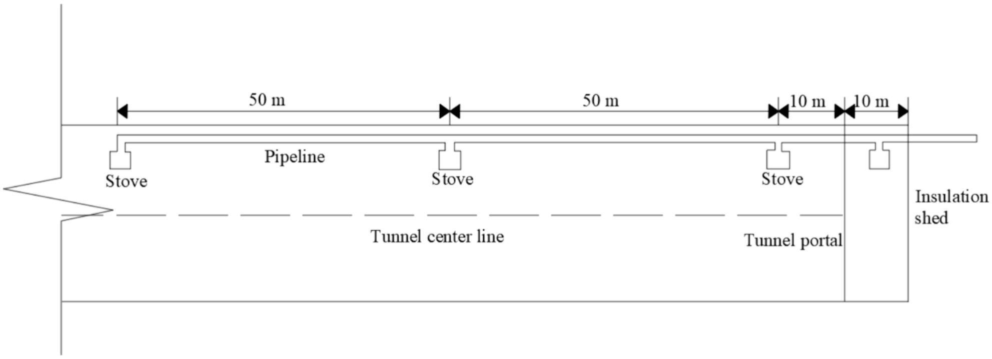

Fig. 2. Thermal method for cold region tunnel concrete curing.

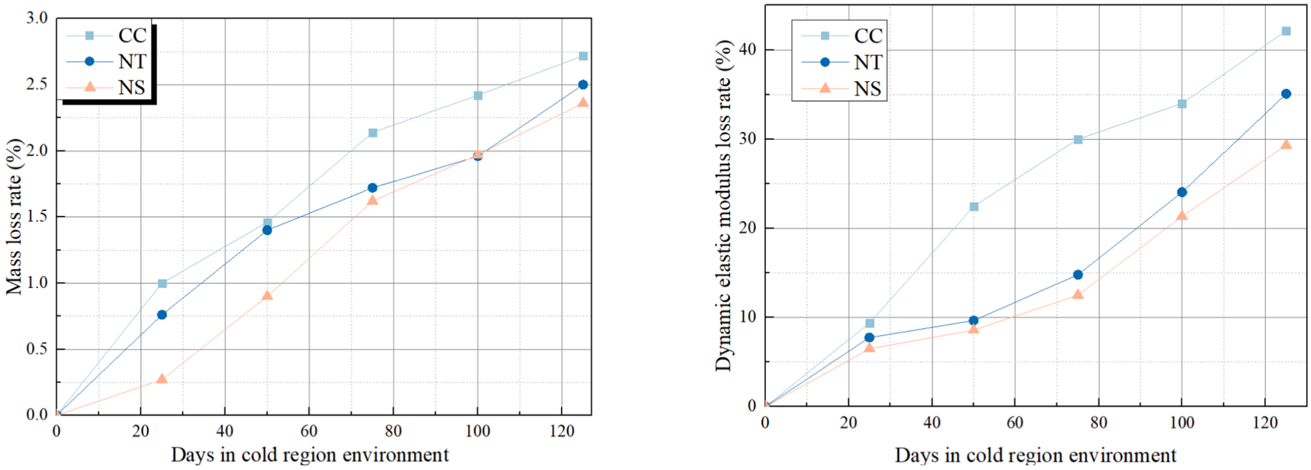

(a) Mass loss of all groups (b) Dynamic elastic modulus loss of all groups

Fig. 4. Macro-performance deterioration of all group concrete specimens.

Table 2
The service life for each group.

MIX. ID	CC	NT	NS
N_F	222	255	252

with similar properties based on their average grayscale values, until there are no more voxels that can be merged. The region growing process was implemented by MATLAB, and its steps are rendered in Fig. 5.

In the region growing algorithm, the selection of seed points plays a crucial role in determining the quality of the segregation results. Therefore, the choice of the pore grayscale threshold in this study is critical and can be found in our previous work [37]. All voxels with grayscale values below this threshold are defined as potential seed points. Subsequently, the region growing algorithm is applied sequentially to those voxels that are seed points and have not yet become growing points. The region growing result are displayed in Fig. 6.

After segmentation of concrete digital images, the pore radii were calculated by count the voxel number. The equivalent radius R_{eq} can be obtained by equivalent pores to a sphere, as follows:

$$R_{eq} = \left(\frac{3}{4\pi}N\right)^{1/3} L_r \tag{1}$$

Where N is the number of voxels in certain pore. And L_r represents the precision of the digital image, that is the true length of the voxels side length, which is 55.6 μm.

To investigate the impact of different nanomaterial modification methods on pore structure under the cold region tunnel environment,

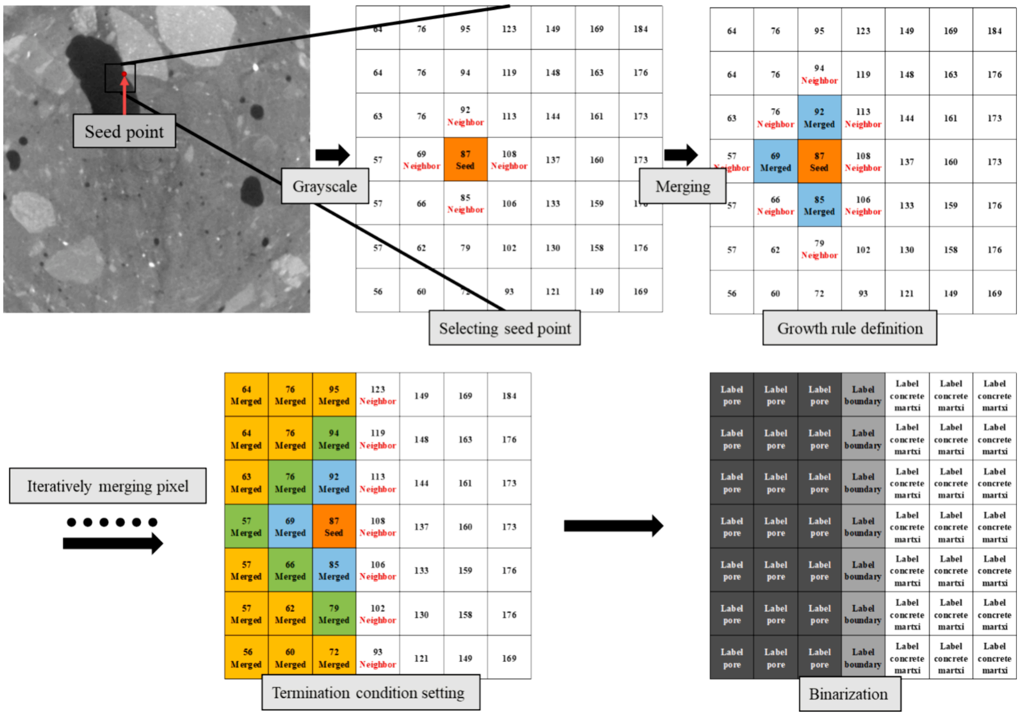

Fig. 5. Region growing algorithm for extracting pores in concrete.

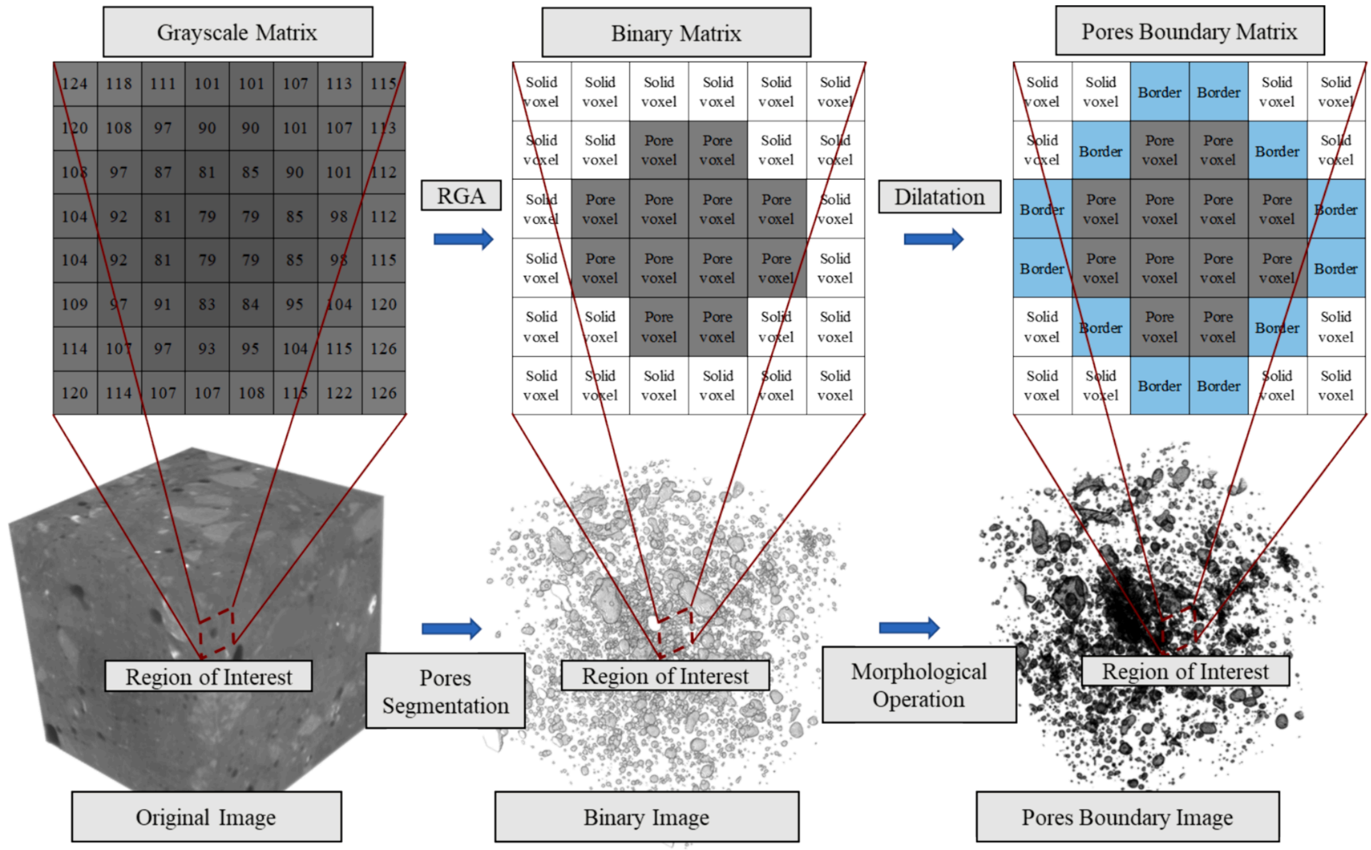

Fig. 6. Pore structure of concrete extracted based on region growing algorithm.

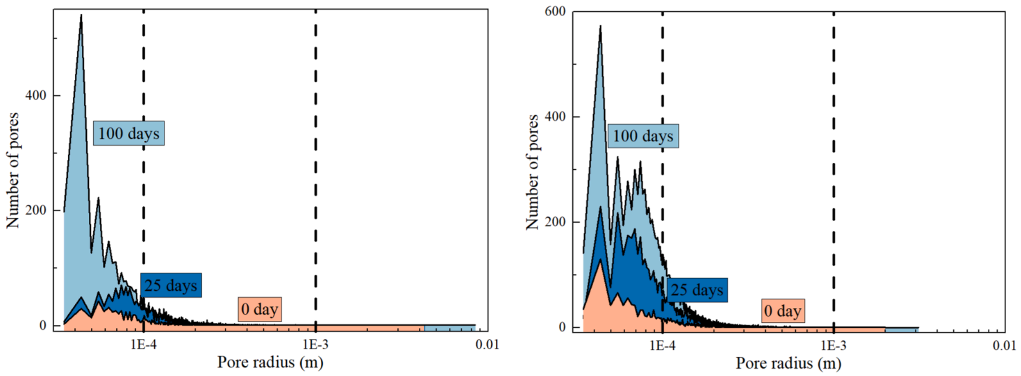

(a) Pore size distribution of group CC (b) Pore size distribution of group NT

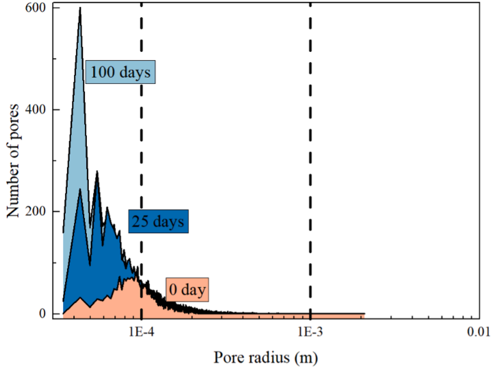

(c) Pore size distribution of group NS

Fig. 7. Pore size distribution (PSD) of all groups.

the pore size distributions of each group under different cold tunnel environment duration were rendered in Fig. 7.

From Fig. 7, it can be observed that as the concrete specimens of each group serve in the cold region tunnel environment, the number of pores with a radius smaller than 100 μm significantly increases. However, for pores with a radius larger than 100 μm, the pore volume remains almost unchanged with increasing service time. This indicates that concrete in the cold region environment is more susceptible to changes in smaller pores. It is worth noting that, although the addition of nanomaterials has little effect on the distribution of pores with a radius smaller than 100 μm, the inclusion of NS and NT effectively inhibits the occurrence of larger pores. From Fig. 7 (a), it can be seen that as the concrete in Group CC service in cold region environment, the maximum pore radius continuously increases. By the service time reaches 100 days, the maximum pore radius has increased from 42.8 mm to 83.9 mm. This is primarily due to the continuous degradation of pore structure in the concrete in the cold region environment, leading to the expansion of existing pores, the emergence of new small pores, and eventually the interconnection between pores, forming larger pores. The presence of such pores often has a significant impact on the performance of concrete. While the inclusion of NS and NT, as rendered in Fig. 7 (b) and (c) cannot suppress the emergence of new small pores, it effectively prevents the interconnection between pores, thus preventing the formation of larger pores. The porosity of each group of concrete within different pore size ranges is shown in Fig. 8.

Fig. 8 further confirms the inhibitory effect of NS and NT on the pore structure of concrete in cold region environments. As shown in the Fig. 8, with the progression of freezing damage, the porosity of pores larger than 1000 μm in nano-modified concrete does not increase significantly. In contrast, the porosity of pores larger than 1000 μm in the group CC increases from 2.08 % to 7.52 %. The porosity of pores smaller than 1000 μm remains relatively unchanged across all groups of concrete as freezing damage progresses. Notably, although the porosity of pores smaller than 100 μm remains at a low level in all conditions, this is primarily due to the limitations of the CT testing resolution. The resolution of the CT test in this study is 55.6 μm, which means that smaller pores in the concrete cannot be detected. For pores that cannot be detected by CT, MIP testing will be used for further investigation.

4.2. Evolution process of pore structure under the cold region tunnel environment based on the digital volume correlation (DVC)

To monitor the changes in pore structure within concrete under the cold region tunnel environment, the Digital Volume Correlation (DVC) method was employed in this study. By comparing digital volume images of concrete under different days of the cold weather conditions with that of the original intact concrete[38]. The DVC method calculates the displacement vectors of voxels on the pore boundaries by tracking the same points in the pre-deformation digital volume image and post-deformation digital volume images [39]. The principle of the DVC method is illustrated in Fig. 9.

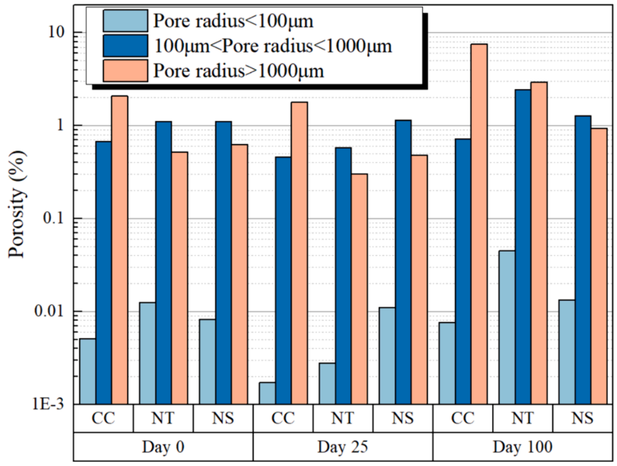

Fig. 8. The porosity of all groups.

As shown in Fig. 9, the pre-deformation digital volume image serves as the reference volume image, denoted as $P(x, y, z)$. The post-deformation digital volume image obtained was adopted as the deformed volume image, denoted as $P(x', y', z')$. The DVC method calculates the 3D displacement vector of each point by tracking the position of discrete points in the reference volume image $P(x,y,z)$. To improve computational efficiency, a small box (sub-volume) centered around the voxel point is typically chosen as the volume image template. The displacement of the voxel is determined by searching for the target sub-volume in the deformed volume image. The target sub-volume has the highest similarity to reference sub-volume template, by moving the sub-volume template voxel by voxel in the deformed volume image. The similarity between the pre-deformation and post-deformation sub-volumes can be described by using Zero-Normalized Cross-Correlation (ZNCC) [40] as expressed:

$$C_{ZNCC} = \frac{\sum_{i=1}^{n}[f(x_i,y_i,z_i) - f_m][g(x_i+u_0,y_i+v_0,z_i+w_0) - g_m]}{\sqrt{\sum_{i=1}^{n}[f(x_i,y_i,z_i) - f_m]^2}\sqrt{\sum_{i=1}^{n}[g(x_i+u_0,y_i+v_0,z_i+w_0) - g_m]^2}} \tag{2}$$

Where $f(x_i,y_i,z_i)$ represents the grayscale value of the i-th voxel in the pre-deformation sub-volume,$g(x_i+u_0,y_i+v_0,z_i+w_0)$ represents the grayscale value of the i-th voxel in the post-deformation sub-volume. f_m represents the average grayscale value in the pre-deformation sub-volume, and g_m represents the average grayscale value in the post-deformation sub-volume. $u_0, v_0,$ andw_0 is the displacement of the voxel to be calculated.

To monitor the changes in pore structure within concrete under the cold region tunnel environment, the boundaries of the pores extracted by using the region-growing algorithm (RGA) in the previous section are considered as $P(x,y,z)$. Through the DVC method, the deformation and shape changes of the pores are calculated, as shown in Fig. 10.

After compiling the changes in all pores within the concrete for each group, the increase in pore volume, θ, in the concrete after a certain number of freeze–thaw cycles (i.e., at 25 days or 100 days of service age) were calculated as shown in the Fig. 11. The increase in pore volume, θ, is defined by Eq. (3).

$$\theta = \frac{\Delta V}{V} \times 100\% \tag{3}$$

Where ΔV represents the increase in the volume of the pore after undergoing a certain number of freeze–thaw cycles. This is calculated by the difference in the number of pixels enclosed by the pore boundary

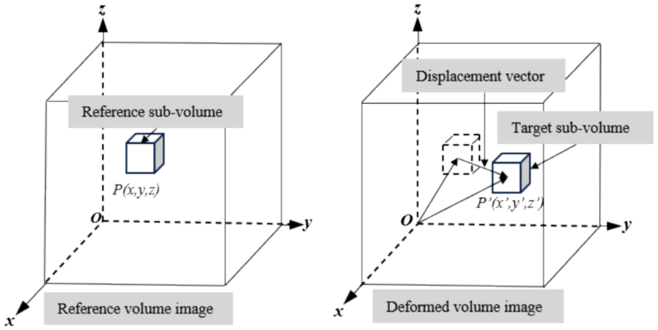

Fig. 9. Principle of the DVC method to calculate the evolution of pore structure.

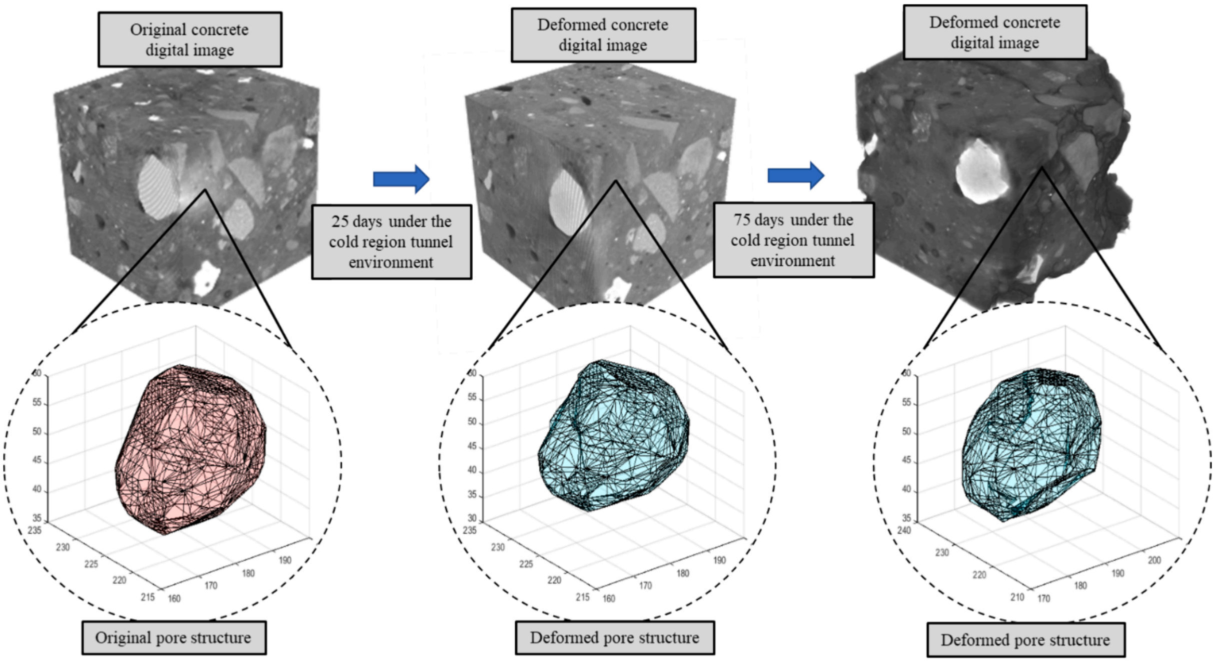

Fig. 10. The deformation and shape changes of the pores.

before and after the freeze–thaw cycles. V represents the volume of the pore before it undergoes freeze–thaw cycles.

In the DVC experimental results, pores with an average ZNCC fitting degree of less than 0.9 at each point on the pore boundary are ignored to eliminate the influence of outliers on the experiment:

Fig. 11 shows the changes in pore volume for the groups CC, NT, and NS. The horizontal axis represents the equivalent radius of the pores in the concrete before experiencing freeze–thaw cycles (i.e., at 0 days of service age), and the vertical axis represents the increase in pore volume in the concrete after a certain number of freeze–thaw cycles (i.e., at 25 days or 100 days of service age). In Fig. 11, after 25 days of the cold region tunnel environment, the increase of pore volume in concrete is very small. It can be seen that in group NS, the average growth rate of pore radius is 5.4 % at 25 days. After 100 days, most of the pore volumes in group NS still changed little, but some pores change also appeared at this time. In this case, the average growth rate of pore radius of group NS is 13.2 %. Concerning to group NT, after 25 days in a cold region environment, the sizes of most pores remained relatively consistent with their pre-deformation sizes. However, some pores exhibited noticeable expansion. At this stage, the average pore radius expansion rate of group NT was 7.4 %. After 100 days, similar to the NS condition, the number of pores showing significant expansion in group NT increased significantly. At this point, the average pore radius growth rate was 19.7 %. Based on the concrete DVC results of group CC, it can be observed that after 25 days of exposure to a cold region environment, the pores exhibiting significant volume changes were the most numerous. The average pore volume expansion rate in group CC after 25 days was 6.4 %. However, after 100 days, due to severe spalling and mass loss in the concrete specimens under group CC, pores with particularly large deformations and significant volume changes had disappeared. This can be seen from the Fig. 11 (a) and (b), where the number of pores decreased significantly.

5. The multi-scale damage evolution based on micromechanical damage model

To investigate the modification mechanism of nanomaterials on concrete in a cold region tunnel environment, this study explores the influence of nanomaterials on the pore structure characteristics of concrete. At the microscale, the expansion stress of the pore wall due to pore water pressure during the freezing process is analyzed, and then the deformation behavior of the pores is calculated. Subsequently, the deterioration process of the pore wall concrete in the cold tunnel environment is studied through micromechanical damage mechanics and a damage accumulation model. Finally, the generalized self-consistent model is used to explore the degradation law of the macroscopic properties of concrete.

5.1. Per-melting dynamics of concrete pore structure during freezing process

The classical thermodynamic principles are employed to describe the solidification process of pore water under negative temperature conditions. At the interface between ice and water, the Gibbs free energy on both sides of the interface should be equal. Consequently, the Gibbs-Duhem equation can be formulated:

$$\frac{\rho_S L(T_m - T_I)}{T_m} = (p_S - p_L) + (p_L - p_m)\left(1 - \frac{\rho_S}{\rho_L}\right) \tag{4}$$

Where ρ_S and ρ_L are the densities of ice and liquid, respectively. T_m, p_m are the solidification temperature and pressure at the reference state. L is the latent heat of phase change. p_S, p_L are the pressure of the ice and liquid. T_I is the temperature at interface between ice and liquid.

The solidification process of pore water is rendered in Fig. 12.

The comprehensive frost heaving theory proposed by Vlahou et al. [41,42] was adopted in this study. During the phase transition between ice and liquid, the temperature remains constant at any location within the ice phase, while the temperature of the liquid phase gradually approaches T_∞ as the radius tends toward R_b. The temperature distribution can be expressed as follows:

$$T_S = T_I(t) \tag{5}$$

$$T_L = \frac{T_I(t) - T_\infty}{r} R_{ice}(t) + T_\infty R_{ice} \le r \le R_b \tag{6}$$

Where T_L and T_S are the temperature of liquid and ice, respectively. R_{ice} represents the radius of ice in pore. R_b is defined as the outer radius of

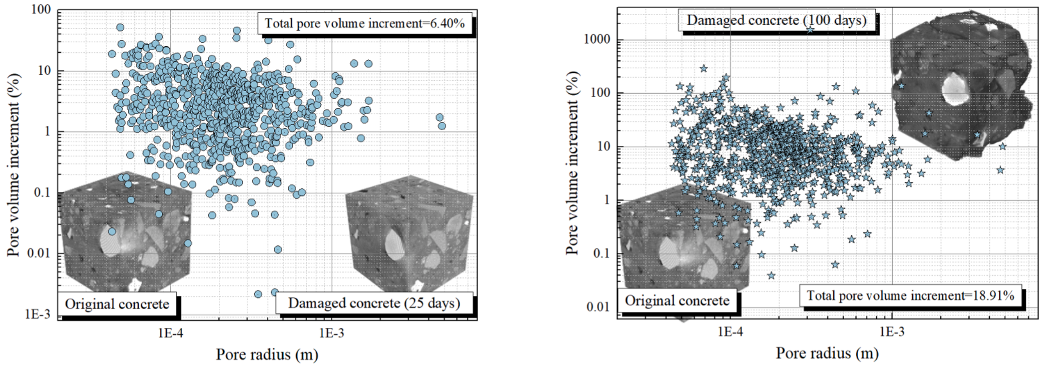

(a) Pore evolution of group CC at 25 days (b) Pore evolution of group CC at 100 days

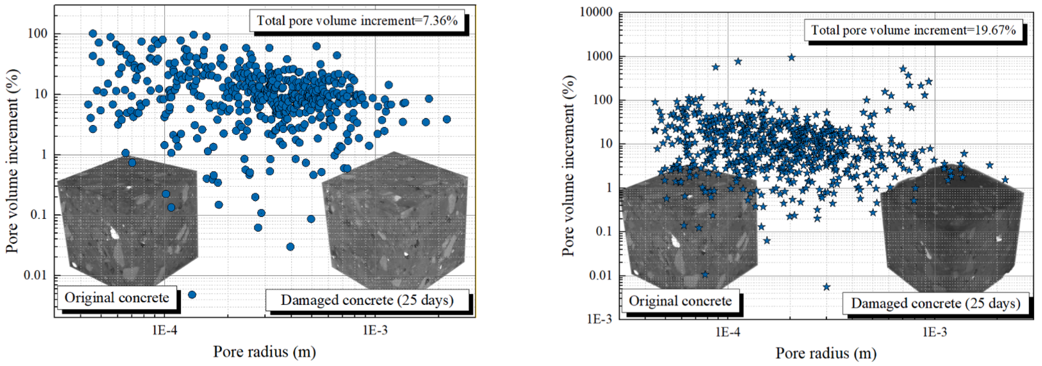

(c) Pore evolution of group NT at 25 days (d) Pore evolution of group NT at 100 days

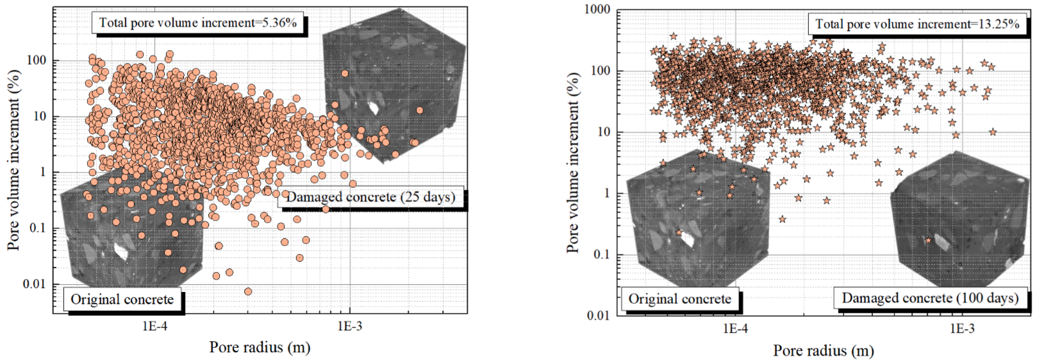

(e) Pore evolution of group NS at 25 days (f) Pore evolution of group NS at 100 days

Fig. 11. The evolution of the pore structure of concrete subjected to different service age.

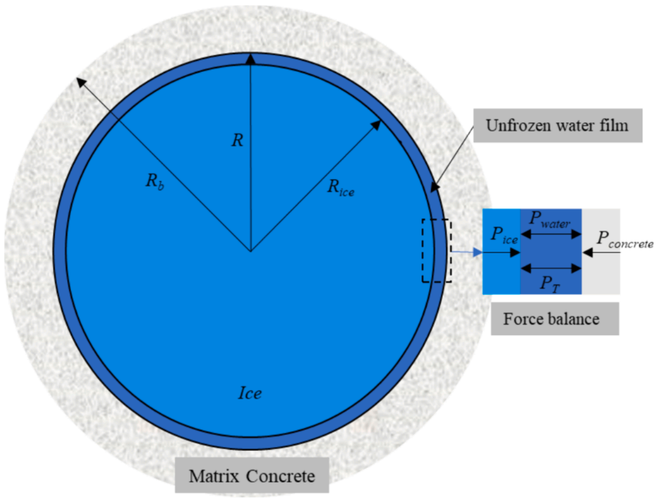

Fig. 12. Schematic diagram of the solidification process in pores.

the matrix concrete from the center of the pore. The value of R_b is based on the CT test results for each condition. It is determined by calculating the Euclidean distance between pores within the concrete.

The interface between ice and liquid during the phase transition of freezing is known as the one-dimensional Stefan Problem [43], wherein at the interface, the heat flux entering from one side must be equal to the heat flux exiting from the other side. Upon considering the latent heat associated with the phase transition between ice and water, the energy balance can be expressed as follows:

$$k_S \frac{\partial T}{\partial r}\bigg|_{r=R_{ice}(t)-} - k_L \frac{\partial T}{\partial r}\bigg|_{r=R_{ice}(t)+} = \rho_S L \frac{dR_{ice}(t)}{dt} \tag{7}$$

Where k_L, k_S is the thermal conductivities of liquid and ice, respectively. ρ_S is the density of ice. L represents the latent heat of water. T and r represent the temperature and distance from the center of the circle at any point in Fig. 12, respectively.

As the volume of ice gradually expands, liquid is compelled towards the porous medium outside the pores, i.e., the concrete, due to the pressure gradient ∇p_l. During this process, the flow of water is governed by Darcy's equation:

$$\mu V = -K \nabla p_l \tag{8}$$

Where μ is the dynamic viscosity coefficient of water, V is the velocity of water, K is the hydraulic permeability of concrete.

Simultaneously, taking into account the mass conservation during the ice expansion process, the expression for the water flow velocity can be derived. The detailed derivation process is presented in Appendix.

$$V(r,t) = \begin{cases} \dfrac{\Delta\rho}{\rho_L} \dfrac{{R_{ice}}^2 \dot{R}_{ice}}{r^2} \; When R_{ice} < r < R \\ \dfrac{\Delta\rho}{\rho_L} \dfrac{{R_{ice}}^2 \dot{R}_{ice}}{r^2} - (1-\phi) \dfrac{R^2 \dot{R}}{r^2} \; When r \geq R \end{cases} \tag{9}$$

Where $\Delta\rho = \rho_L - \rho_S$; ϕ is the porosity of matrix concrete; R is the radius of pore.

By substituting Eq. (9) into Eq. (8), the water pressure within the pore can be obtained. Within the pores, the pressure of the liquid phase is assumed to be uniform everywhere. Therefore, the water pressure inside the liquid phase becomes equal to the water pressure within the porous medium when $r = R$:

$$p_l(r,t) = \begin{cases} \dfrac{\mu}{K} \left[\dfrac{\Delta\rho}{\rho_L} \dfrac{{R_{ice}}^2 \dot{R}_{ice}}{R} - (1-\phi) R \dot{R} \right] When R_{ice} < r \leq R \\ \dfrac{\mu}{K} \left[\dfrac{\Delta\rho}{\rho_L} \dfrac{{R_{ice}}^2 \dot{R}_{ice}}{r} - (1-\phi) \dfrac{R^2 \dot{R}}{r} \right] When R < r \leq R_b \end{cases} \tag{10}$$

When the radius of the ice gradually approaches the pore radius, i.e., $R_{ice} \rightarrow R$, a thin layer of unfrozen water film exists within the pore wall with a thickness of $h = R - R_{ice}$. This film exerts pressure, denoted as p_T, on both the pore wall and the ice. At this point, the pressures on both sides of the ice-water interface are related as follows:

$$p_T = p_S - p_l \tag{11}$$

At the same time, the deformation of the pore space at this stage cannot be neglected, i.e., $\dot{R} \neq 0$. Substituting Eq. (10) into Eq. (4) allows for the computation of the temperature at the ice-water interface:

$$T_I = T_m \left(1 - \frac{\Delta\rho}{\rho_L \rho_S L} p_l - \frac{1}{\rho_S L} p_T + \frac{\Delta\rho}{\rho_L \rho_S L} P_m \right) \tag{12}$$

Substituting the interface temperature T_I into the Stefan condition, as rendered in Eq. (7), at the ice-water interface. Therefore, the growth control equation for the ice at this point:

$$\rho_S L R_{ice} \dot{R}_{ice} = k_L \Delta T - \frac{T_m k_L}{\rho_S L} p_T - \frac{\Delta\rho k_L T_m}{\rho_L \rho_S L} p_l + \frac{\Delta\rho T_m k_L}{\rho_L \rho_S L} P_m \tag{13}$$

Where $\Delta T = T_m - T_\infty$ is denoted as the cooling intensity.

When incorporating Eq. (11) we have:

$$p_T = E_c \left(\frac{R}{R_0} - 1 \right) - \frac{\Delta\rho\mu}{\rho_L K R} {R_{ice}}^2 \dot{R}_{ice} + \frac{(1-\phi)\mu}{K} R \dot{R} \tag{14}$$

Where E_c is the effective elastic modulus; R_0 is the initial radius of pore.

$$E_c = E \frac{{R_b}^2 - {R_0}^2}{(1-\nu){R_0}^2 + (1+\nu){R_b}^2} \tag{15}$$

Where E and ν are the elastic modulus and the poisons' ratio of concrete matrix, respectively.

From Eqs. (10), (13) and (14), it is evident that when $\dot{R}_{ice} = 0$ and $\dot{R} = 0$, the pore and ice reaches its maximum, attaining an equilibrium state. Thus, solving for the equilibrium state yields the pore radius:

$$R_{eq} = R_0 \left(1 + \frac{\Delta T L \rho_S}{T_m E_c} + \frac{\Delta\rho P_m}{\rho_L E_c} \right) \tag{16}$$

5.2. The micromechanical damage model for concrete pore structure during freezing process

The concentric layered Represented Area Element (RAE) model [44] was adopted to depict the impact of expansion stress during the freezing on the pore structure and the encapsulation concrete layer. The basic configuration of the concentric layered RAE model is illustrated in Fig. 13.

In this model, it is assumed that the expansion stress resulting from the phase transition in two adjacent pores does not mutually influence each other. This assumption holds validity, particularly when the porosity of concrete is relatively low, implying a significant distance between adjacent RAE pores. During the progress of the water–ice phase transition, the ice within the pore gradually expands, exerting stress on the pore walls, consequently leading to the deformation of the pore. At this stage, the encapsulation concrete layer can be divided into two parts, i.e., the damaged zone and the elastic zone as indicated in Fig. 14.

For the concrete in the elastic zone, elastic mechanics were employed. However, for the concrete in the damaged zone, a damage factor denoted as D_ε to characterize the extent of damage. Based on the Fig. 14, the boundary conditions are as follows:

$$\begin{cases} \sigma_r = -P_{eff}, when r = R \\ D_\varepsilon = 0, \sigma_r = -P_c, \varepsilon_\theta = \varepsilon_t, when r = R_c \end{cases} \tag{17}$$

Where P_{eff} is the effective stress induced on the pore wall during the phase transition. P_c and R_c is the effective stress and radius at the interface between the elastic zone and the damaged zone, respectively. ε_t is the ultimate tensile strain of concrete. σ_r and ε_θ are the radial stress and circumferential strain, respectively.

Assuming that when the circumferential strain ε_θ of concrete exceeds the ultimate tensile strain ε_t, the concrete enters the damage stage. At this point, the constitutive model for concrete is described by the Mazar damage model, with the damage factor D_ε given by:

$$D_\varepsilon = 1 - \frac{\varepsilon_t (1 - A_T)}{\varepsilon_\theta} - \frac{A_T}{exp[B_T(\varepsilon_\theta - \varepsilon_t)]} \tag{18}$$

Where A_T and B_T are the parameters of the Mazar damage model.

For concrete in the elastic zone, due to its symmetry, the governing equation in polar coordinates can be expressed as:

$$\frac{d\sigma_r}{dr} + \frac{\sigma_r - \sigma_\theta}{r} = 0 \tag{19}$$

Where σ_θ is the circumferential stress.

Based on the governing equation and boundary conditions, the corresponding forms of stress and strain are given by:

$$\begin{cases} \sigma_r = \dfrac{P_c {R_c}^2}{{R_b}^2 - {R_c}^2} \left(1 - \dfrac{{R_b}^2}{r^2} \right) \\ \sigma_\theta = \dfrac{P_c {R_c}^2}{{R_b}^2 - {R_c}^2} \left(1 + \dfrac{{R_b}^2}{r^2} \right) \end{cases} \tag{20}$$

$$\begin{cases} \varepsilon_r = \dfrac{(1+\nu)}{E} \dfrac{P_c {R_c}^2}{{R_b}^2 - {R_c}^2} \left(1 - 2\nu - \dfrac{{R_b}^2}{r^2} \right) \\ \varepsilon_\theta = \dfrac{(1+\nu)}{E} \dfrac{P_c {R_c}^2}{{R_b}^2 - {R_c}^2} \left(1 - 2\nu + \dfrac{{R_b}^2}{r^2} \right) \end{cases} \tag{21}$$

Where ν is the Poisson's ratio of concrete and E is the modulus of elasticity of concrete; ε_r is the radial strain.

For concrete in the damaged zone, the radial displacement u satisfies the following governing equation:

$$\frac{d^2u}{dr^2} + \frac{1}{r}\frac{du}{dr} - (1 - D_\varepsilon)\frac{u}{r^2} = 0 \tag{22}$$

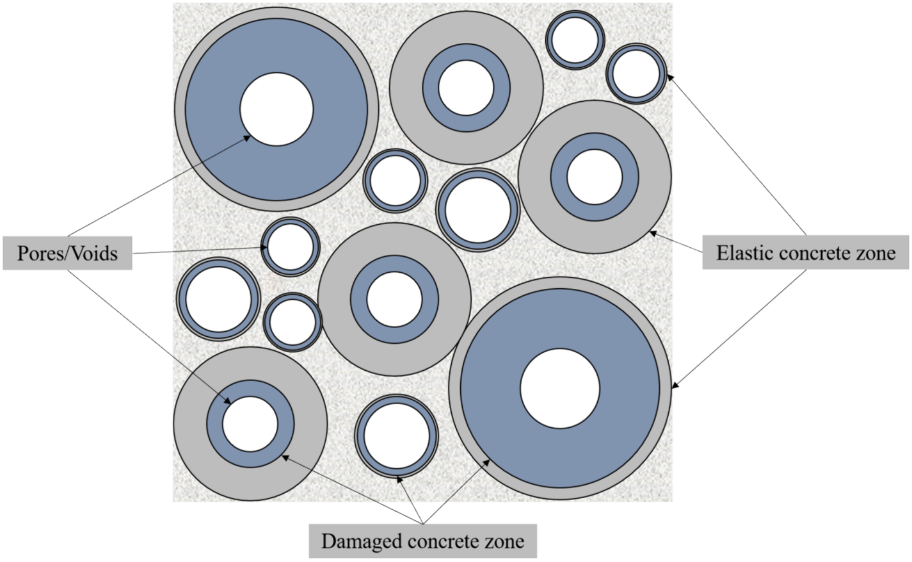

Fig. 13. Schematic diagram of the concentric layered Represented Area Element model.

Solving the aforementioned governing equation yields:

$$u = C_1 r^{\sqrt{1-D_\varepsilon}} + C_2 r^{-\sqrt{1-D_\varepsilon}} \tag{23}$$

Where C_1 and C_2 are the integration constants, which need to be determined through boundary conditions.

Based on the geometric equation, the strain of concrete in the damage zone can be expressed as:

$$\begin{cases} \varepsilon_r = C_1\sqrt{1-D_\varepsilon}\, r^{\sqrt{1-D_\varepsilon}-1} - C_2\sqrt{1-D_\varepsilon}\, r^{-\sqrt{1-D_\varepsilon}-1} \\ \varepsilon_\theta = C_1 r^{\sqrt{1-D_\varepsilon}-1} + C_2 r^{-\sqrt{1-D_\varepsilon}-1} \end{cases} \tag{24}$$

Simultaneously, considering the strain compatibility principle at the interface between the damage zone and the elastic zone:

$$\begin{cases} C_1\sqrt{1-D_\varepsilon}\, {R_c}^{\sqrt{1-D_\varepsilon}-1} - C_2\sqrt{1-D_\varepsilon}\, {R_c}^{-\sqrt{1-D_\varepsilon}-1} = \dfrac{(1+\nu)}{E}\dfrac{P_c {R_c}^2}{{R_b}^2 - {R_c}^2}\left(1 - 2\nu - \dfrac{{R_b}^2}{{R_c}^2}\right) \\ C_1 {R_c}^{\sqrt{1-D_\varepsilon}-1} + C_2 {R_c}^{-\sqrt{1-D_\varepsilon}-1} = \dfrac{(1+\nu)}{E}\dfrac{P_c {R_c}^2}{{R_b}^2 - {R_c}^2}\left(1 - 2\nu + \dfrac{{R_b}^2}{{R_c}^2}\right) \end{cases} \tag{25}$$

Hence, the integration constants C_1 and C_2 can be determined as:

$$\begin{cases} C_1 = \dfrac{(1+\nu)}{E}\dfrac{P_c {R_c}^2}{{R_b}^2 - {R_c}^2}(1-2\nu) \\ C_2 = \dfrac{(1+\nu)}{E}\dfrac{P_c {R_c}^2}{{R_b}^2 - {R_c}^2}{R_b}^2 \end{cases} \tag{26}$$

At the interface between the damaged zone and the elastic zone, considering that the circumferential strain satisfies $\varepsilon_\theta = \varepsilon_t$, we have:

$$\frac{(1+\nu)}{E}\frac{P_c {R_c}^2}{{R_b}^2 - {R_c}^2}\left(1 - 2\nu + \frac{{R_b}^2}{{R_c}^2}\right) = \varepsilon_t \tag{27}$$

At the pore boundary, the radial displacement should satisfy:

$$u_{r=R} = C_1 R^{\sqrt{1-D_\varepsilon}} + C_2 R^{-\sqrt{1-D_\varepsilon}} \tag{28}$$

By simultaneously considering Eqs. (16), (27), and (28), the damaged zone radius, R_c, can be solved.

5.3. Damage accumulation model of high and low cycle fatigue combination under the cold region environment

For concrete under the cold region tunnel environment, it is evident that the strain of concrete in the damaged zone significantly exceeds its elastic limit. In the fatigue model, the stress induced by pore water during the ice-water phase transition causes the circumferential strain near the pores in the matrix concrete to significantly exceed the concrete's ultimate tensile strain (defined as the damage zone). In contrast, the circumferential strain in the matrix concrete far from the pores has not yet exceeded the ultimate tensile strain (defined as the elastic zone). At this point, the fatigue modes of concrete in the elastic zone and damage zone are different. Thus, two fatigue modes, proposed by Li et al [45], are used to describe the fatigue damage process of the elastic modulus in the elastic zone and damage zone of the matrix concrete.

Assuming that the damage accumulation $D(N)$ remains constant over one fatigue cycle, considering the boundary conditions $N = 0$ when $D = 0$, and $N = N_F$ when $D = 1$, the fatigue damage evolution equation for damage and elastic zone concrete can be written in Eqs. (29) and (30), respectively.

$$D_d(N) = 1 - \left[1 - \left(\frac{N}{N_F}\right)^{1-c}\right]^{\frac{1}{b+1}} \tag{29}$$

$$D_e(N) = 1 - \left[1 - \frac{N}{N_F}\right]^{\frac{1}{b+1}} \tag{30}$$

When $c = 0$, the fatigue damage in damage zone $D_d(N)$ degenerates into the fatigue damage in elastic zone $D_e(N)$. Therefore, after one day of cold region tunnel environment, the bulk modulus for the damaged and elastic zone concrete can be calculated based on elastic modulus: $K_d =$

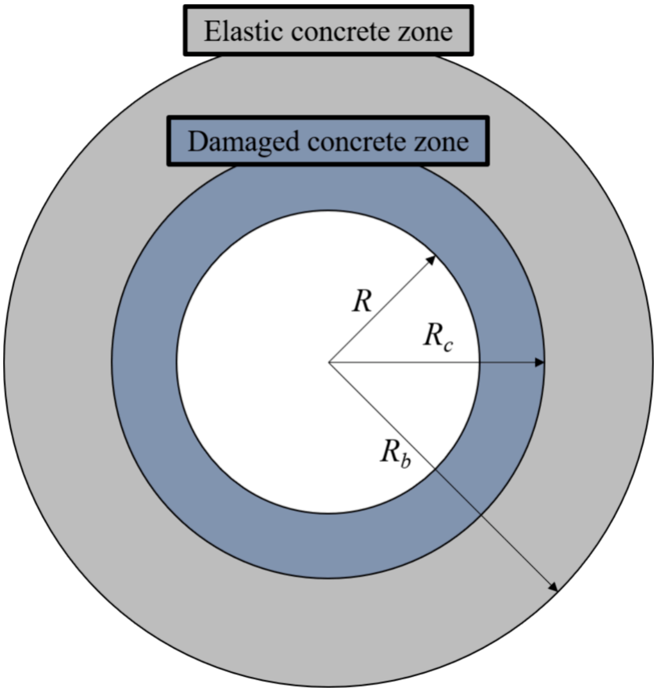

Fig. 14. Schematic diagram of concrete deterioration at the freezing process.

$(1 - D_d)E_0/3(1 - 2\nu)$ and $K_e = (1 - D_e)E_0/(3 - 6\nu)$, respectively. Subsequently, the generalized self-consistent model based on Mori-Tanaka homogenization scheme [46] was adopted, which involves conceptualizing the porous material as composed of spherical voids embedded in a homogeneously solid matrix. The generalized self-consistent model was adopted to calculate the effective elastic modulus of the combination of encapsulation concrete layer and pore as rendered in Fig. 15.

The bulk modulus K of this composite material 01 can be expressed in the form

$$K_{01} = K_1 + \frac{c_{01}(K_0 - K_1)(3K_1 + 4G_1)}{3K_1 + 4G_1 + 3(1 - c_{01})(K_0 - K_1)} \tag{31}$$

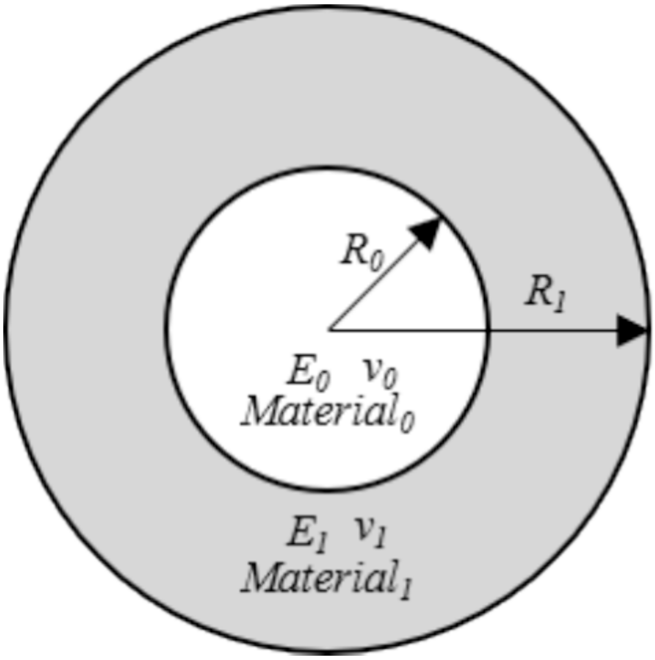

Fig. 15. The generalized self-consistent model of two different materials.

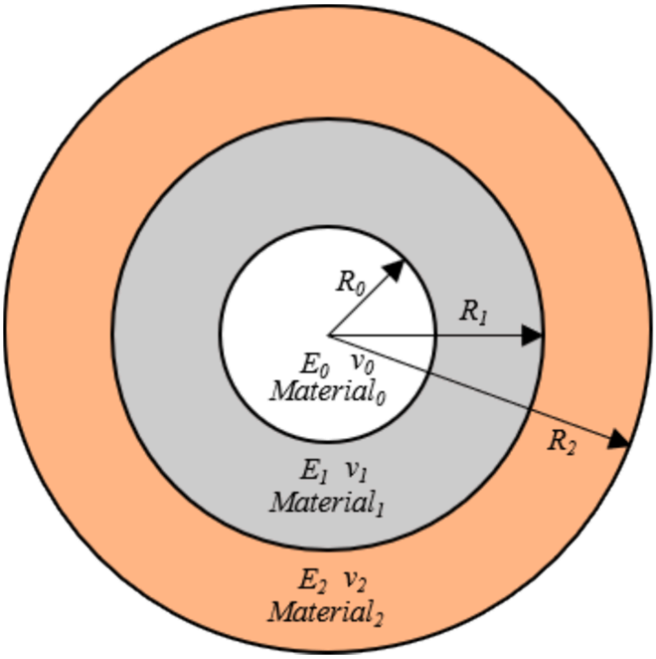

Fig. 16. The generalized self-consistent model of concrete under fatigue damage.

Where $c_{01} = {R_0}^3/{R_1}^3$ represents the volume fraction of material 0 in the composite material 01, and G_1 represents the shear modulus of material 1.

For concrete that has undergone fatigue damage, it should be considered as a composite material composed of three different phases, i.e., pores, damaged concrete, and undamaged concrete, as illustrated in the Fig. 16:

To determine the material parameter K_{12} for the composite material composed of material 1 and material 2, the Eq. (31) was still used for calculation. The bulk modulus K_{012} of the material, formed by the combination of materials 0, 1, and 2, can be expressed as a combination of material 0 and material 12, as well as a combination of material 01 and material 2. Therefore, we have:

$$\begin{aligned} K_{012} &= K_{12} + \frac{c_{02}(K_0 - K_{12})(3K_{12} + 4G_{12})}{3K_{12} + 4G_{12} + 3(1 - c_{02})(K_0 - K_{12})} \\ &= K_2 + \frac{c_{12}(K_{01} - K_2)(3K_2 + 4G_2)}{3K_2 + 4G_2 + 3(1 - c_{12})(K_{01} - K_2)} \end{aligned} \tag{32}$$

Where $c_{02} = {R_0}^3/{R_2}^3$ represents the volume fraction of material 0 in the composite material 012, $c_{12} = {R_1}^3/{R_2}^3$ represents the volume fraction of material 01 in the composite material 012.

Based on Eq. (32), the effective bulk modulus K_{12} of composite material 12 can be obtained. Simultaneously, assuming that the Poisson's ratio of concrete remains constant, i.e., $\nu_2 = \nu_1 = \nu$, and K_{12} in the equation is independent of the bulk modulus of the material within the pores. By solving Eq. (32), the effective bulk modulus K_{12} of composite material 12 can be obtained after one fatigue cycle:

$$K_{12} = \frac{K_{012}(3c_{02} + 4b)}{4b(1 - c_{02})} \tag{33}$$

$$b = \frac{3(1 - 2\nu)}{2(1 + \nu)}$$

Building upon the aforementioned concept, the elastic modulus evolution of the encapsulation concrete layer under the cold region tunnel environment can be ultimately determined. During freezing process, concrete located in the damage zone not only experiences fatigue damage D_L resulting from the fatigue damage, but also endures damage D_ε from phase transition. To account for the combination of these two types of damage, a general form of the stress–strain relationship for damaged concrete is considered as:

$$\sigma = E_{ini}(1 - D_L)(1 - D_\varepsilon)\varepsilon = E_{ini}(1 - D_m)\varepsilon \tag{34}$$

Therefore, the total damage factor for the concrete in the damaged zone can be obtained as:

$$D_m = D_L + D_\varepsilon - D_L D_\varepsilon \tag{35}$$

For computational convenience, it is assumed that the damage incurred by concrete in the damage zone during the phase transition is a constant value, with this value being taken at the pore wall, i.e., $D_\varepsilon = D_\varepsilon(R)$.

6. Numerical application and discussion

To determine the deformation of pores during the phase transition of pore water, Eq. (16) is employed. The parameter values necessary for the per-melting dynamics model are presented in Table 3.

It should be noted that the elastic modulus E of the concrete matrix in Eq. (16) gradually decreases with an increasing fatigue cycle number, and this value is difficult to directly measure. Therefore, to reasonably infer the elastic modulus of the concrete matrix, the generalized self-consistent model is still employed, as depicted in Fig. 15. Here, the concrete is considered a composite material consisting of a concrete matrix (with a bulk modulus of *K1*) and pores (with a bulk modulus of *K2*), resulting in a composite bulk modulus of *K12*. Subsequently, Eq. (31) is used to calculate the bulk modulus *K1* of the concrete matrix, given the total bulk modulus of the concrete (*K12*). The elastic modulus of the concrete of all group is shown in Table 4.

In Eq. (31), c_{01} represents the porosity of the concrete. It is important to note that the porosity of the concrete should not be solely determined by the porosity obtained from the Region Growing Algorithm of the digital images from CT scans. Due to the limitations of CT resolution, pores with a radius smaller than 35 μm cannot be segmented from the images. Therefore, the porosity of the concrete under various conditions in this study is composed of three parts: The first part is the porosity of the cement paste obtained through the Mercury Intrusion Porosimetry (MIP), with specific values provided in our previous study [37]. The second part is the voids in the concrete obtained from CT scans. The third part is the porosity of the aggregates. Since this study assumes that aggregates do not contain pores, the porosity is considered to be 0. To calculate the total porosity of the concrete, it is also necessary to use image segmentation methods to calculate the volume fractions of the cement paste and aggregates in the concrete digital images. The total porosity of all group concrete is shown in Table 5.

For the Mazar damage model parameters A_T and B_T defined in Eq. (18), the typical ranges for these values for general concrete materials are $0.7 \le A_T \le 1$, $10^4 \le B_T \le 10^5$. Therefore, in this study, $A_T = 0.7$, $B_T = 10^4$ were adopted in this study. In the micromechanical damage model, by solving Eqs. (27) and (28) simultaneously, the radius of the damaged zone R_c can be obtained. The elastic zone radius R_b, as introduced earlier, is determined by the interval between pores within the concrete. As shown in the Fig. 6, after extracting all pore voxels using the Region Growing Algorithm, the Euclidean distance from each pore to its nearest neighbor was calculated. Half of this distance is then taken as the elastic zone radius R_b, and adopted in micromechanical damage model. The pore interval distribution for each group is provided in the Fig. 17.

Table 3
Typical values for the parameter used in the analysis.

Parameter	Symbol	Value	Unit
Latent heat	L	334×10^3	$m^2\ s^{-2}$
Thermal conductivity	k_l	2	$kg\ m\ s^{-3}\ K^{-1}$
Density of ice	ρ_s	0.92×10^3	$kg\ m^{-3}$
Density of water	ρ_l	10^3	$kg\ m^{-3}$
Temperature change	ΔT	18	K
Melting temperature	T_m	273	K
Reference state pressure	P_m	1	atm
Poisson's ratio	ν	0.2	Dimensionless
Ultimate tensile strain of concrete	ε_t	3×10^{-3}	Dimensionless

Table 4
The elastic modulus of all group (GPa).

MIX. ID	CC	NT	NS
Elastic modulus	29.76	30.49	30.78

Table 5
The total porosity of all groups.

MIX. ID	Porosity of cement paste%	Volume fracture of cement paste%	Volume fracture of aggregate %	Volume fracture of air void %	Total porosity %
CC	16.80	82.29	14.95	2.76	13.85
NT	15.40	81.64	16.63	1.73	12.59
NS	15.00	83.15	15.10	1.75	12.49

From Fig. 17, it can be observed that for the majority of pores, their interspacing is significantly larger than their respective radii. Therefore, the assumption that the pore interspacing is sufficiently large, and the mutual interaction of frost forces between pores can be neglected, is considered reasonable. In Eq. (30), the parameters of the concrete fatigue damage model are crucial for the process of pore structure failure. To determine the parameters c and b, the parameter fitting using the dynamic modulus loss data for each group was conducted. The experimental damage factor for each condition can be expressed as $D = 1 - \frac{E_d(N)}{E_{d0}}$, where E_{d0} is the initial dynamic modulus of elasticity of concrete before damage. Fitting the relative dynamic modulus data in Fig. 4 (b) using Eq. (30), the fitting parameters for each condition are obtained and shown in Table 6.

The aforementioned computational process was implemented by using MATLAB. Firstly, utilizing Eq. (16), the pore radius when the ice expands to a steady state is calculated. By solving Equations (16), (27), and (28) simultaneously, the radius of the damaged zone (R_c) under the freezing state can be obtained. When the ice inside the pore melts, at this point, the elastic strain of the concrete fully recovers. The increase in the pore radius due to the irreversible residual deformation is then calculated as $R + u_p$. Additionally, at this moment, considering that the concrete in the damaged zone undergoes fatigue damage, the elastic modulus of the encapsulation concrete can be calculated using Eq. (33). Repeating these steps, the variation in the concrete pore structure and the degradation process of the elastic modulus can be obtained, ultimately.

After compiling the changes in all pores within the concrete for each group, a comparison is made with the simulated results, as shown in the Fig. 11. The horizontal axis represents the equivalent radius of pores in concrete before undergoing freeze–thaw cycles (i.e., at 0 days of service age), and the vertical axis represents the equivalent radius of pores in concrete after a certain number of freeze–thaw cycles (i.e., at 25 days or 100 days of service age). In the DVC experimental results, pores with an average ZNCC fitting degree of less than 0.9 at each point on the pore boundary are ignored to eliminate the influence of outliers on the experiment:

In Fig. 18, the analysis results are in good agreement with the experimental results. Therefore, the proposed micromechanical damage model appears suitable for the predictions of the evolution of concrete pore structure under the cold region tunnel environment. Based on the proposed multi-scale damage evolution model, the degradation process

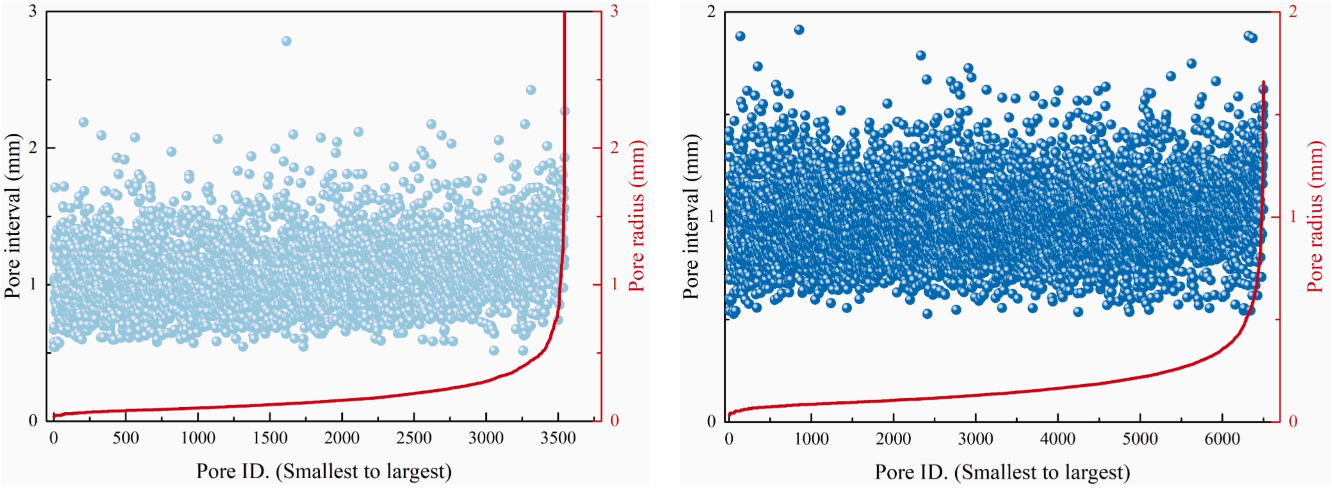

(a) Pore interval distribution of Group CC

(b) Pore interval distribution of Group NT

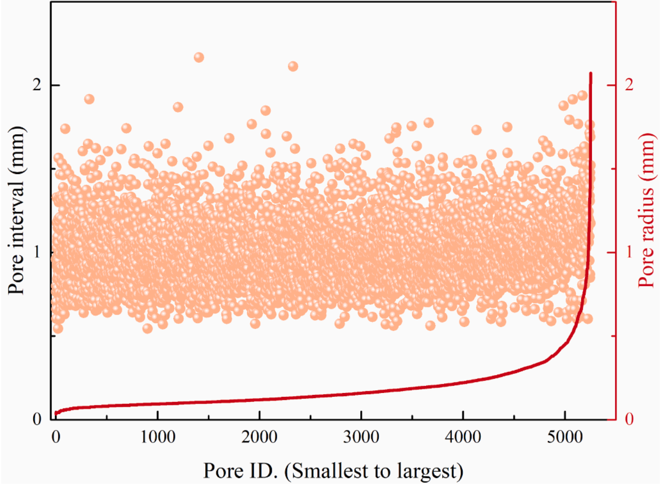

(c) Pore interval distribution of Group NS

Fig. 17. Pore interval distribution (PID) of all groups.

Table 6
The fatigue damage model parameters for each group.

MIX. ID	CC	NT	NS
c	0.342	0	0
b	3.393	2.736	3.598
R^2	0.9833	0.9519	0.9628

of the elastic modulus and the development of pore structure in concrete specimens under cold region tunnel environments were studied. Additionally, the elastic modulus, pore expansion, and damage zone radius in RAE elements of different sizes were analyzed. The PSD and PID for each group are sourced from Fig. 7 and Fig. 17, respectively. The increase in porosity and elastic modulus are shown in Fig. 19.

From Fig. 19 (a), it can be observed that the elastic modulus of Group CC decreases rapidly, with a decrease of 52.25 % after 200 days, from 29.74 GPa to 14.20 GPa. Group NT and Group NS exhibit decreases in elastic modulus of 33.62 % and 28.98 %, respectively, after 200 days. Additionally, it is evident that the degradation pattern of elastic modulus in Group CC is significantly different from that in Group NT and Group NS. This difference is mainly due to variations in the parameters of the fatigue damage model for each group. From Fig. 19 (b), it can be seen that in the early stage of freezing damage, the overall pore volume expansion rates in concrete for each group are relatively similar. However, in the later stage of freezing damage, there are substantial differences in the pore volume expansion rates for each group. The pore expansion rate in Group CC concrete reaches 70.9 %, while in Group NT and Group NS concrete, the pore expansion rates are relatively smaller, at 65.9 % and 62.9 %, respectively.

Nano-silica particles, due to their high activity and substantial surface area, can significantly enhance the performance of cement-based materials. The mechanisms of nano-silica modification effects are included [16,47,48]: (1) Chemical Activity: Due to the extremely small diameter of nanoparticles and their large specific surface area, they possess high surface energy and contact area. (2) Filling Effect: Cement concrete structures contain numerous microscopic pores caused by water evaporation or uneven particle distribution. The ultra-fine nanomaterial particles typically have a diameter of less than 20 nm, allowing them to effectively fill these micropores, thereby reducing the microscopic porosity, improving the pore structure, and increasing the density of the cement paste. (3) Nucleation Effect: Based on the nucleation principle, ultra-fine nanoparticles provide suitable nucleation sites for crystal growth. Cement and mineral admixtures coat the nanomaterials, allowing for rapid hydration growth. This process occurs in two stages: the nucleation stage, where nanoparticles act as centers adsorbing other particles, and the hydration growth stage, where nanoparticles react with minerals or hydration products in the cement to form stable gels. The growth of this gel occurs around the embedded nanoparticles, ultimately forming a dense and uniform C-S-H gel.

In order to reveal the degradation mechanisms of different condi-

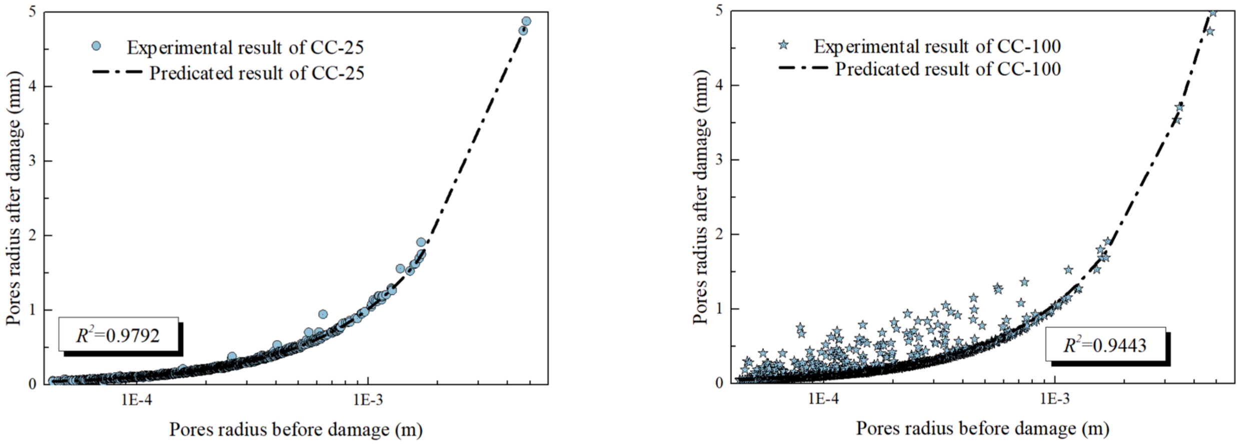

(a) Pore evolution of group CC at 25 days (b) Pore evolution of group CC at 100 days

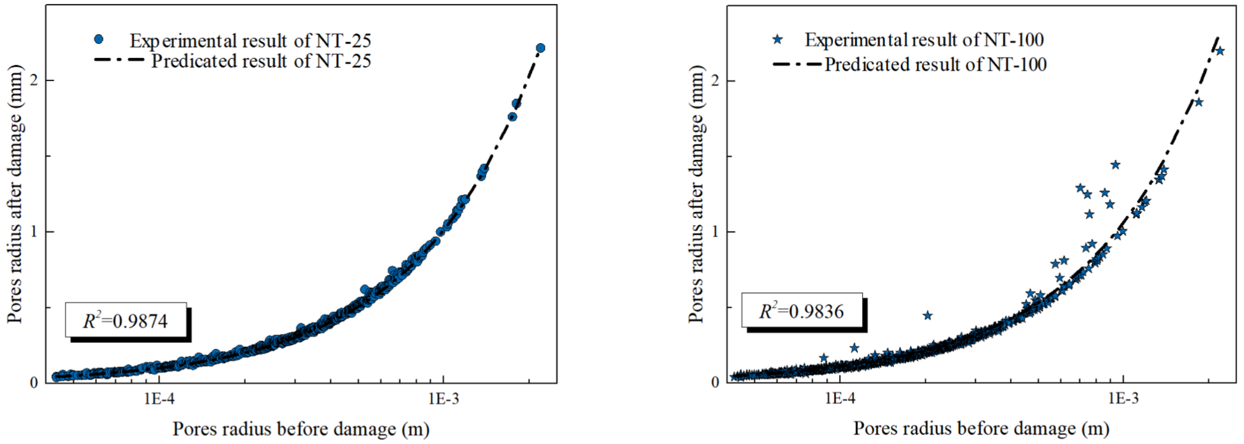

(c) Pore evolution of group NT at 25 days (d) Pore evolution of group NT at 100 days

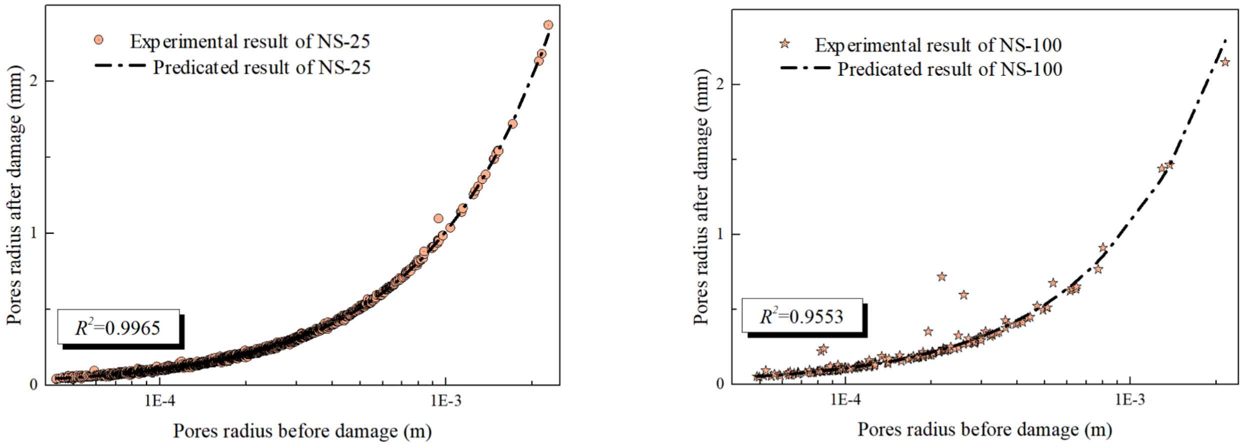

(e) Pore evolution of group NS at 25 days (f) Pore evolution of group NS at 100 days

Fig. 18. The evolution of the pore structure of concrete subjected to different age of cold region environment.

tions in cold region tunnel environments from the perspective of individual RAE elements, the reduction rates of elastic modulus, pore volume expansion rates, and ratio of damage concrete radius R_c to the RAE radius R_b, which characterizes the proportion of damaged concrete in the RAE element, are listed in Fig. 20 for each group at the freezing damage age of 200 days.

From Fig. 20 (a), it can be seen that in the cold region environment after 200 days, the reduction rates of elastic modulus of RAE elements in concrete for each group increase gradually with the increase of pore radius in RAE element. This indicates that the damage suffered by the RAE elements occupied by larger pores is greater than that by smaller pores, leading to a lower elastic modulus of the RAE elements at 200 days of freezing damage. It can also be observed that the RAE elements in the NT and NS groups, where nanomaterials are incorporated, exhibit significantly higher elastic modulus values compared to the CC group. From Fig. 20 (b), it can be seen that in each group, there is a significant expansion in the pore volume within the RAE elements of concrete after experiencing 200 days in the cold region environment. It can also be observed that the pore volume expansion rates of RAE elements with different pore radii are essentially the same, with only minor fluctuations. This implies that pore volume expansion is not the main factor leading to the reduction in elastic modulus of RAE elements with larger

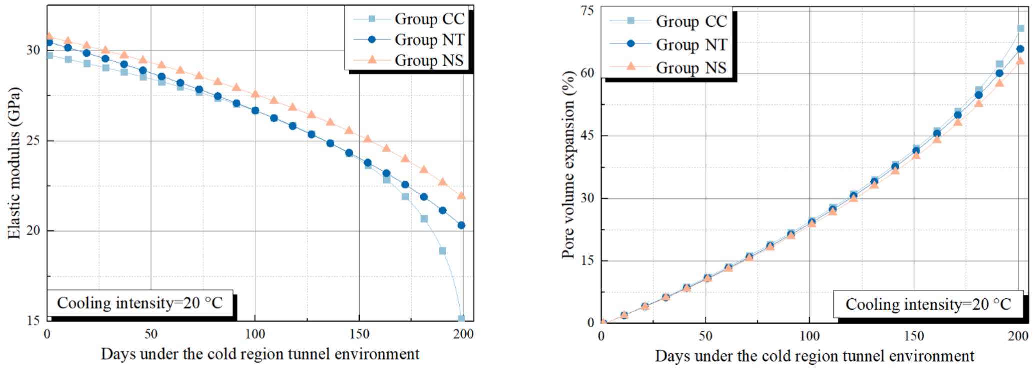

(a) The initial elastic modulus on elastic modulus (b) The initial elastic modulus on pore expansion

Fig. 19. The macro-performance deterioration of all groups based on the micromechanical damage model.

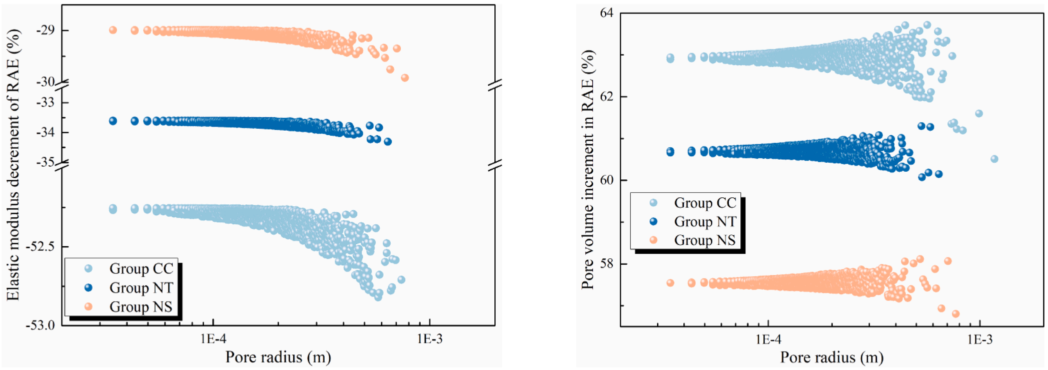

(a) The decrement of RAE elastic modulus (b) The pore volume expansion in RAE

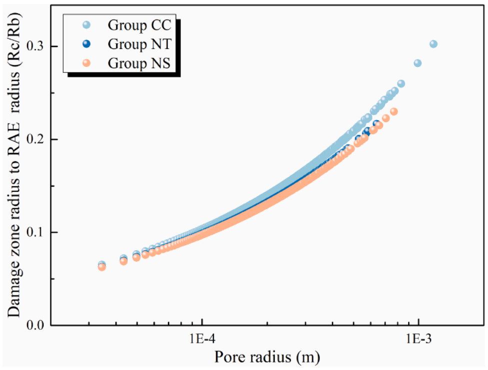

(c) The ratio of damage zone radius to radius of RAE

Fig. 20. The performance evolution of RAE elements.

pore radii. The ratio of the damage zone concrete radius R_c to the undamaged zone concrete radius R_b in the RAE elements of each group gradually increases with the increase of pore radius in the RAE elements, as rendered in Fig. 20 (c). Moreover, the trends of the values of R_c/R_b for each group are the same as the pore radius changes. In fact, this is mainly because, as shown in the pore interval distribution (PID) curve in Fig. 17, the intervals between pores of different sizes are generally in the range of 0.5–1.5 mm. With the increase of pore size, the proportion of the pore portion in the RAE elements becomes larger, while the concrete encasement layer that inhibits pore expansion becomes smaller. This results in the damage zone concrete radius R_c generated when water inside the pores freezes and expands becoming closer to the RAE element radius. In fact, there are often a large number of small pores surrounding large pores in concrete, with the small pores being very close to the large pores and separated only by a thin layer of cement paste. This leads to the gradual integration of these small pores with the large pores through the cracks after the large pores are subjected to the pressure of freezing pore water. In RAE elements with smaller pore radii, the damage zone concrete radius R_c generated by the freezing of pore water is smaller, and the proportion of the pore volume in the RAE elements is also smaller. Therefore, after the cold region environment, the main component of the RAE elements is still the undamaged zone concrete. Although larger pores in concrete often cause more severe damage, their quantity is relatively small. On the other hand, small pores are abundant in concrete and are important components of the pore structure. Therefore, the overall reduction in elastic modulus of concrete is still dominated by RAE elements with smaller pores.

7. Conclusion

In this study, the service environment of concrete in a simulated cold region tunnel was modeled, and in-situ CT scanning was employed to monitor the evolution of pores in different nano-modified concretes over time. The study provides useful insights into the application of nanomaterials for improving concrete durability in cold regions. While nano-materials may be relatively expensive, their use in critical sections of infrastructure can significantly enhance performance and longevity, justifying the cost for key engineering projects. Key innovations and findings from the study include:

(1) Significant differences in failure modes were revealed through mass and resonant frequency testing after nano-material modification. Concrete modified with nano-silica (NS) and nano-titanium (NT) exhibited longer service lives compared to the control group (CC). Digital volume images indicated that while the control concrete showed continuous increases in small pores and the expansion of large pores, the nano-modified concretes effectively inhibited the connection of large pores with small pores. This prevention of larger harmful pore formation was more pronounced after 100 days, demonstrating the effectiveness of nano-materials in suppressing pore volume expansion in cold region environments.

(2) A novel micromechanical fatigue-damage coupled analysis model was developed to investigate the impact of pore water crystallization on concrete pore structures. Utilizing pre-melting dynamic theory, the model analyzed the expansion stress on pore walls during water crystallization. By dividing the concrete into undamaged and damaged zones, elastic mechanics were applied to undamaged zones and damage mechanics to damaged zones. Both low-cycle and high-cycle fatigue were employed to describe the reduction in elastic modulus, and the generalized self-consistent model was used to study the overall modulus.

(3) The analysis of RAE elements of different sizes revealed that the elastic modulus deterioration was more significant in elements with large pores due to the thinner concrete encapsulation layer. However, as small pores constituted a larger proportion of the volume, the overall elastic modulus of concrete was still dominated by the performance changes of RAE elements with small pores. This finding underscores the critical role of pore size distribution in the durability and mechanical properties of concrete under cold region conditions.

CRediT authorship contribution statement

Wei Xia: Writing – review & editing, Writing – original draft, Visualization, Supervision, Software, Methodology, Investigation, Formal analysis, Data curation. **Wei-kang Li:** Data curation, Formal analysis, Software. **Jia-rui Rao:** Visualization, Validation. **Zong-quan Jiang:** Project administration, Funding acquisition. **Jiann-wen Woody Ju:** Writing – review & editing, Validation, Supervision, Conceptualization. **Sheng-ai Cui:** Supervision, Resources, Project administration, Funding acquisition, Conceptualization.

Declaration of competing interest

The authors declare that they have no known competing financial interests or personal relationships that could have appeared to influence the work reported in this paper.

Data availability

Data will be made available on request.

Acknowledgements

We acknowledge the National Natural Science Foundation of China, China (No. 52278277), the International Science and Technology Cooperation Program of Sichuan Province, China (No. 2023YFH0061), the Central Government Funds of Guiding Local Scientific and Technological Development for Sichuan Province, China (No. 2021ZYD0045), the Geotechnical and Underground Engineering Intelligent Construction and Safety Overseas Expertise Introduction Center for Discipline Innovation, China (No. B2101120223101), and the Fundamental Research Funds for the Central Universities, China (No. 2682021GF020) This work was supported by a grant from the China Scholarship Council, China (No. 528390).

Appendix

As rendered in Fig. 21, consider a pore with a radius R containing ice with a radius R_{ice}, and the remaining space in the pore filled with liquid water. At this point, the radius of the ice increases by dR_{ice}. Simultaneously, due to the pressure exerted by pore water on the pore wall, the pore radius also increases by dR. Analyze the mass conservation of water on the enveloping surface at a radius r (where $r > R$). The mass change of water within the enveloping surface at this moment is composed of two parts: one arising from the density difference between ice and water and the other from pore expansion. Therefore, it can be expressed as:

$$4\pi r^2 V(r,t)\rho_L = \left[\frac{4}{3}\pi\left(\dot{R}_{ice}+R_{ice}\right)^3 - \frac{4}{3}\pi {R_{ice}}^3\right]\Delta\rho - \left[\frac{4}{3}\pi\left(\dot{R}+R\right)^3 - \frac{4}{3}\pi R^3\right](1-\phi)\rho_L \tag{36}$$

The first term on the left side of the equation represents the mass flux of water through the enveloping surface with a radius of r. The first term on the right side of the equation signifies the reduction in water mass within the enveloping surface due to ice expansion. The second term on the right side represents the increase in water mass within the enveloping surface caused by pore expansion. Simplifying the equation and neglecting higher-order terms, we obtain:

$$r^2 V(r,t)\rho_L = {R_{ice}}^2\dot{R}_{ice}\Delta\rho - R^2\dot{R}(1-\phi) \tag{37}$$

Ultimately, it can be expressed as:

$$V(r,t) = \frac{\Delta\rho}{\rho_L}\frac{{R_{ice}}^2\dot{R}_{ice}}{r^2} - \frac{R^2\dot{R}}{r^2}(1-\phi), r > R \tag{38}$$

When $r < R$, the second term on the right side of the equation, representing the mass increase caused by pore expansion, vanishes. Therefore, it can be written as:

$$V(r,t) = \frac{\Delta\rho}{\rho_L}\frac{{R_{ice}}^2\dot{R}_{ice}}{r^2}, r < R \tag{39}$$

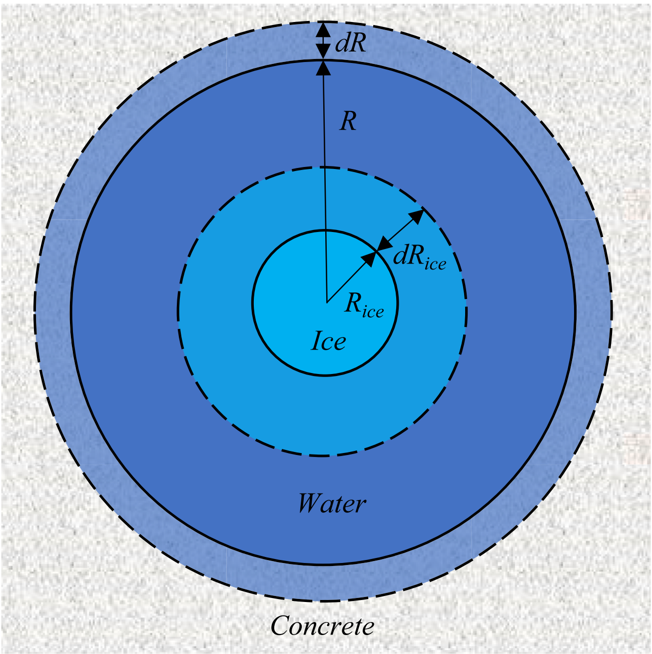

Fig. 21. Derivation of the velocity of water based on the mass conservation.

References

[1] Cui S, Liu P, Li Z, Xu X, Woody Ju J. Shotcrete performance-loss due to seepage and temperature coupling in cold-region tunnels. Constr Build Mater 2020;246:118488. https://doi.org/10.1016/j.conbuildmat.2020.118488.

[2] Hartwich P, Vollpracht A. Influence of leachate composition on the leaching behaviour of concrete. Cem Concr Res 2017;100:423–34. https://doi.org/10.1016/j.cemconres.2017.07.002.

[3] Sun K, Jia J, Zhi X, Wu J, Liu Y, Wei Y. Investigation of hydro-thermal variations and mechanical properties in cold region tunnels under long-term freeze–thaw cycles. Tunn Undergr Space Technol 2024;143:105469. https://doi.org/10.1016/j.tust.2023.105469.

[4] Lin Z, Xia C, Zhou S, Du S. Experimental investigation of the temperature field of a frost-penetration tunnel based on a whole life cycle laboratory test. Tunn Undergr Space Technol 2023;142:105378. https://doi.org/10.1016/j.tust.2023.105378.

[5] Walder JS, Hallet B. A theoretical model of the fracture of rock during freezing. Geol Soc Am Bull 1985;96:336. https://doi.org/10.1130/0016-7606(1985)96%3C336:atmotf%3E2.0.co;2.

[6] Hori M, Morihiro H. Micromechanical analysis on deterioration due to freezing and thawing in porous brittle materials. Int J Eng Sci 1998;36:511–22. https://doi.org/10.1016/s0020-7225(97)00080-3.

[7] Taber S. The Mechanics of Frost Heaving. J Geol 1930;38:303–17. https://doi.org/10.1086/623720.

[8] Everett DH. The thermodynamics of frost damage to porous solids. Trans Faraday Soc 1961;57:1541–51. https://doi.org/10.1039/TF9615701541.

[9] Víctor Agmo Hernández. An overview of surface forces and the DLVO theory. ChemTexts 2023;9. https://doi.org/10.1007/s40828-023-00182-9.

[10] Scherer GW. Crystallization in pores. Cem Concr Res 1999;29:1347–58. https://doi.org/10.1016/s0008-8846(99)00002-2.

[11] Coussy O. Poromechanics of freezing materials. J Mech Phys Solids 2005;53:1689–718. https://doi.org/10.1016/j.jmps.2005.04.001.

[12] Hall K. The role of thermal stress fatigue in the breakdown of rock in cold regions. Geomorphology 1999;31:47–63. https://doi.org/10.1016/s0169-555x(99)00072-0.

[13] Du M, Jing H, Gao Y, Su H, Fang H. Carbon nanomaterials enhanced cement-based composites: advances and challenges. Nanotechnol Rev 2020;9:115–35. https://doi.org/10.1515/ntrev-2020-0011.

[14] Marinho B, Ghislandi M, Tkalya E, Koning CE, de With G. Electrical conductivity of compacts of graphene, multi-wall carbon nanotubes, carbon black, and graphite powder. Powder Technol 2012;221:351–8. https://doi.org/10.1016/j.powtec.2012.01.024.

[15] Liu M, Xiao H, Li R, Liu J. Dispersion characteristics of various contents of nano-TiO2 and its effect on the properties of cement-based composite. Struct Concr 2018;19:1301–8. https://doi.org/10.1002/suco.201800110.

[16] Li H, Xiao H, Yuan J, Ou J. Microstructure of cement mortar with nano-particles. Compos B Eng 2004;35:185–9. https://doi.org/10.1016/S1359-8368(03)00052-0.

[17] Madani H, Bagheri A, Parhizkar T. The pozzolanic reactivity of monodispersed nanosilica hydrosols and their influence on the hydration characteristics of Portland cement. Cem Concr Res 2012;42:1563–70. https://doi.org/10.1016/j.cemconres.2012.09.004.

[18] Rai S, Tiwari S. Nano Silica in Cement Hydration, Materials Today. Proceedings 2018;5:9196–202. https://doi.org/10.1016/j.matpr.2017.10.044.

[19] Singh LP, Karade SR, Bhattacharyya SK, Yousuf MM, Ahalawat S. Beneficial role of nanosilica in cement based materials – A review. Constr Build Mater 2013;47:1069–77. https://doi.org/10.1016/j.conbuildmat.2013.05.052.

[20] Land G, Stephan D. The influence of nano-silica on the hydration of ordinary Portland cement. J Mater Sci 2011;47:1011–7. https://doi.org/10.1007/s10853-011-5881-1.

[21] Yu R, Spiesz P, Brouwers HJH. Effect of nano-silica on the hydration and microstructure development of Ultra-High Performance Concrete (UHPC) with a low binder amount. Constr Build Mater 2014;65:140–50. https://doi.org/10.1016/j.conbuildmat.2014.04.063.

[22] Joshaghani A, Balapour M, Mashhadian M, Ozbakkaloglu T. Effects of nano-TiO2, nano-Al2O3, and nano-Fe2O3 on rheology, mechanical and durability properties of self-consolidating concrete (SCC): An experimental study. Constr Build Mater 2020;245:118444. https://doi.org/10.1016/j.conbuildmat.2020.118444.

[23] Wang J, He L, Wu X, Zhang L. Influence of nanoparticles on age-associated mechanical properties of cement asphalt mortar. Constr Build Mater 2021;301:124033. https://doi.org/10.1016/j.conbuildmat.2021.124033.

[24] Mousavi MA, Sadeghi-Nik A, Bahari A, Jin C, Ahmed R, Ozbakkaloglu T, et al. Strength optimization of cementitious composites reinforced by carbon nanotubes and Titania nanoparticles. Constr Build Mater 2021;303:124510. https://doi.org/10.1016/j.conbuildmat.2021.124510.

[25] Moro C, Hala El Fil V, Francioso M-L. Influence of water-to-binder ratio on the optimum percentage of nano-TiO2 addition in terms of compressive strength of mortars: A laboratory and virtual experimental study based on ANN model. Constr Build Mater 2021;267:120960. https://doi.org/10.1016/j.conbuildmat.2020.120960.

[26] He S, Chai J, Yang Y, Cao J, Qin Y, Xu Z. Effect of nano-reinforcing phase on the early hydration of cement paste: A review. Constr Build Mater 2023;367:130147. https://doi.org/10.1016/j.conbuildmat.2022.130147.

[27] Xia W, Cui S, Zhu L, Li W, Ju JW, Wang X. Effects of nano-silica modification on early age hydration process in winter construction of tunnel engineering. Constr Build Mater 2023;408:133804. https://doi.org/10.1016/j.conbuildmat.2023.133804.

[28] Onaizi AM, Huseien GF, Lim NHAS, Amran M, Samadi M. Effect of nanomaterials inclusion on sustainability of cement-based concretes: A comprehensive review. Constr Build Mater 2021;306:124850. https://doi.org/10.1016/j.conbuildmat.2021.124850.

[29] Monteiro H, Moura B, Soares N. Advancements in nano-enabled cement and concrete: Innovative properties and environmental implications. Journal of Building Engineering 2022;56:104736. https://doi.org/10.1016/j.jobe.2022.104736.

[30] Goel G, Sachdeva P, Chaudhary AK, Singh Y. The use of nanomaterials in concrete: A review, Materials Today. Proceedings 2022;69:365–71. https://doi.org/10.1016/j.matpr.2022.09.051.

[31] Hu Z, Ding H, Lai J, Wang H, Wang X, He S. The durability of shotcrete in cold region tunnel: A review. Constr Build Mater 2018;185:670–83. https://doi.org/10.1016/j.conbuildmat.2018.07.088.

[32] National railway administration standard for acceptance of concrete work in railway. TB 10424-2018, Beijing, 2019.

[33] F. Fu, Research performance improvement of shotcrete for tunnel portal in cold region, Southwest Jiaotong university. (2019). (In Chinese).

[34] Standard for test methods of long-term performance and durability of ordinary concrete. GB/T 50082-2009, Beijing, 2009.

[35] Li Q, Wei Z, Zhao C. Optimized Automatic Seeded Region Growing Algorithm with Application to ROI Extraction. International Journal of Image and Graphics 2017; 17:1750024. https://doi.org/10.1142/s0219467817500243.

[36] Hashemi MA, Ghonwa Khaddour F, Baudin T, Massart SS. A tomographic imagery segmentation methodology for three-phase geomaterials based on simultaneous region growing. Acta Geotech 2013;9:831–46. https://doi.org/10.1007/s11440-013-0289-5.

[37] Cui S, Xia W, Zeng G, Cao Z, Li G, Ju JW. Nano-modification effect on the pore characteristics and the water multiscale transport properties of concrete in winter construction of tunnel engineering. Cem Concr Compos 2023;137:104933. https://doi.org/10.1016/j.cemconcomp.2023.104933.

[38] Tian Y, Jiang H, Fan X, Zhang G, Jin N, Zeng Q, et al. Corrosion damages of reinforced concrete characterized by X-ray CT and DVC techniques. Constr Build Mater 2023;409:134218. https://doi.org/10.1016/j.conbuildmat.2023.134218.

[39] Chateau C, Nguyen TT, Bornert M. Julien Yvonnet, DVC-based image subtraction to detect microcracking in lightweight concrete. Strain 2018;54. https://doi.org/10.1111/str.12276.

[40] Holmes JW, Silvano Sommacal R, Das Z, Stachurski PC. Digital image and volume correlation for deformation and damage characterisation of fibre-reinforced composites: A review. Compos Struct 2023;315:116994. https://doi.org/10.1016/j.compstruct.2023.116994.

[41] Ioanna Vlahou M. Grae Worster, Ice growth in a spherical cavity of a porous medium. J Glaciol 2010;56:271–7. https://doi.org/10.3189/002214310791968494.

[42] Ioanna Vlahou, M. Grae Worster, Freeze fracturing of elastic porous media: a mathematical model, Proceedings of the Royal Society A: Mathematical, Physical and Engineering Sciences. 471 (2015) 20140741–20140741. https://doi.org/10.1098/rspa.2014.0741.

[43] Qu L-H, Ling F, Xing L. Numerical study of one-dimensional Stefan problem with periodic boundary conditions, Thermal Science/Thermal. Science 2013;17:1453–8. https://doi.org/10.2298/tsci1305453q.

[44] Zhou S. Jiann-Wen Woody Ju, A chemo-micromechanical damage model of concrete under sulfate attack. Int J Damage Mech 2021;30:105678952199791. https://doi.org/10.1177/1056789521997916.

[45] Li SC, Xu J, Tao YQ, Tang XJ, Yang HW. Low cycle fatigue damage model and damage variable expression of rock. Rock Soil Mech 2009;30. https://doi.org/10.16285/j.rsm.2009.06.047 (in Chinese).

[46] Mori T, Tanaka K. Average stress in matrix and average elastic energy of materials with misfitting inclusions. Acta Metall 1973;21:571–4. https://doi.org/10.1016/0001-6160(73)90064-3.

[47] Ji T. Preliminary study on the water permeability and microstructure of concrete incorporating nano-SiO2. Cem Concr Res 2005;35:1943–7. https://doi.org/10.1016/j.cemconres.2005.07.004.

[48] Li H, Xiao H, Ou J. A study on mechanical and pressure-sensitive properties of cement mortar with nanophase materials. Cem Concr Res 2004;34:435–8. https://doi.org/10.1016/j.cemconres.2003.08.025.